Available online at www.sciencedirect.com
SCIENCE DIRECT®
Journal of Computational Physics 198 (2004) 580–616
JOURNAL OF COMPUTATIONAL PHYSICS
www.elsevier.com/locate/jcp

# Discretization errors in large eddy simulation: on the suitability of centered and upwind-biased compact difference schemes

Noma Park, Jung Yul Yoo, Haecheon Choi *

*School of Mechanical and Aerospace Engineering, Seoul National University, Seoul 151-744, Republic of Korea*

Received 30 July 2003; accepted 22 January 2004
Available online 3 March 2004

**Abstract**

The suitability of high-order accurate, centered and upwind-biased compact difference schemes for large eddy simulation (LES) is evaluated through the static and dynamic analyses. For the static error analysis, the power spectra of the finite-differencing and aliasing errors are evaluated in the discrete Fourier space, and for the dynamic error analysis LES of isotropic turbulence is performed with various dissipative and non-dissipative schemes. Results from the static analysis give a misleading conclusion that both the aliasing and finite-differencing errors increase as the numerical dissipation increases. The dynamic analysis, however, shows that the aliasing error decreases as the dissipation increases and the finite-differencing error overweighs the aliasing error. It is also shown that there exists an optimal upwind scheme of minimizing the total discretization error because the dissipative schemes decrease the aliasing error but increase the finite-differencing error. In addition, a classical issue on the treatment of nonlinear term in the Navier–Stokes equation is revisited to show that the skew-symmetric form minimizes both the finite-differencing and aliasing errors. The findings from the dynamic analysis are confirmed by the physical space simulations of turbulent channel flow at $Re = 23000$ and flow over a circular cylinder at $Re = 3900$.


*PACS:* 02.70.Bf; 02.30.Nw; 47.27.Eq

*Keywords:* Large eddy simulation; Discretization error; Finite-differencing error; Aliasing error; Numerical dissipation; Compact upwind scheme; Modified wavenumber; Turbulent channel flow; Flow over a circular cylinder

## 1. Introduction

Large eddy simulation (LES) has been regarded as a viable engineering tool for turbulent flow rather than a research tool in accordance with rapidly enhanced computer architecture and mathematical mod-

* Corresponding author. Tel.: +82-2-880-8361; fax: +82-2-878-3662.
*E-mail addresses:* noma@plume.snu.ac.kr (N. Park), jyyoo@plaza.snu.ac.kr (J.Y. Yoo), choi@socrates.snu.ac.kr (H. Choi).

0021-9991/$ - see front matter 
doi:10.1016/j.jcp.2004.01.017

eling [1]. It has been especially true since the advent of advanced subgrid-scale (SGS) models with sound physical basis, e.g. dynamic model [2,3] or SGS estimation model [4].

It is widely accepted that LES is more sensitive to the accuracy of spatial discretization scheme than direct simulation, because LES is performed on grids that are just fine enough to resolve large flow structures so that scales near the cut-off wavenumber are still energetic. Therefore, resolved scales should not be artificially dissipated nor contaminated by the discretization errors in order to get accurate SGS stresses. Although the Fourier spectral method may be the optimal choice of meeting this requirement, most of challenging applications for LES are those in complex geometries where spectral methods are of limited use. For such applications, more conventional methods such as finite difference or finite volume methods have to be used.

The numerical discretization errors can be divided into two categories, or the finite-differencing error and the aliasing error, which have different origins. The finite-differencing error comes from the numerical approximation of spatial derivatives which can be best understood by the concept of modified wavenumber (MWN) in the Fourier space. On the other hand, the aliasing error arises whenever nonlinear terms are approximated in the discrete physical space as the point-wise product [5–10].

Some recent a priori and a posteriori tests [7–11] with finite difference schemes show that the discretization error may outweigh the contribution from the SGS force, and the aliasing error is the leading source of errors for high-order schemes but the finite-differencing error becomes dominant for low-order schemes.

On the other hand, there has been a renewed interest on high-order upwind schemes such as weighted essentially non-oscillatory (WENO) schemes [12,13], compact upwind schemes [14,15] and plenty of their variants [16–18]. The need for developing high-order upwind schemes arises when the problems with strong discontinuity are to be tackled such as the flow with shock/turbulence and shock/boundary layer interaction. Besides, it is believed that upwind schemes have the ability of reducing the aliasing error due to embedded numerical dissipation.

However, it became clear in recent years that dissipative schemes are not good candidates for use in LES of turbulent flow. A representative example is LES of flow past a circular cylinder performed by Beaudan and Moin [19] (denoted as BM94 hereinafter) at the Reynolds number of 3900, where fifth- and seventh-order upwind schemes were used. Although these schemes have been successfully used for DNS of transitional flow over a flat plate [20], the conclusion of BM94 is that the numerical dissipation overwhelms the contribution from the SGS force. This conclusion was again confirmed by Mittal and Moin [21].

Nevertheless, there have been plenty of researches that investigated the use of upwind schemes for LES [22–28], where two different approaches were taken in using upwind schemes for LES. The first is to use upwind schemes in the conventional LES formalism with the same SGS model used for non-dissipative difference schemes. The second is to use the dissipative error of upwind schemes as the built-in SGS models without introducing any explicit models, which is referred to as monotone integrated large-eddy simulation (MILES) [23,27,28]. When one of these approaches is adopted, upwind schemes should satisfy one of the following conditions [23]: (1) their numerical dissipation should be much lower than the physical SGS dissipation (condition C1), or (2) their numerical dissipation should be able to produce the appropriate amount of SGS dissipation (condition C2). The investigation of the condition C1 in the context of the conventional LES formalism is the main concern of the present study. The concept of MILES and condition C2 will be briefly addressed later in this paper.

Results from LES over a circular cylinder with QUICK scheme [22] and from LES/MILES of isotropic turbulence [23] and fully developed channel flow [24] with shock-capturing schemes support the conclusion of BM94. However, the conclusions made by Ladeinde et al. [25] and Meinke et al. [26] are quite different from that of BM94. For example, Meinke et al. [26] reported, through the simulations of turbulent channel flow and spatially evolving jet, that the results with AUSM [29] and sixth-order compact scheme combined with compact filter show negligible difference.

From the survey of the previous studies of using upwind schemes for LES (and MILES), we draw the following conclusions:

- There exists a rough consensus that the numerical dissipation strongly affects large structures on resolved scales as well as unresolved turbulence.
- For all simulations, however, numerical and physical parameters such as grid resolution, numerical dissipation and SGS dissipation are mixed up in a complex way such that it is difficult to assess the effect of numerical dissipation in a systematic manner.
- The interpretation of the numerical results depends mainly on *a posteriori* tests. The numerical method as well as the discretization error should be quantified for a systematic analysis.

In this regard, some useful methodologies for the definition of numerical errors and SGS forces have been proposed [7–10]. In the present study, those methodologies are extended and applied to evaluate the effect of numerical dissipation on the solution of resolved scales. From the present investigation, we hope to answer the following questions:

(i) Is the conclusion by BM94 applicable to other schemes such as recently developed high-order upwind schemes?
(ii) Does the numerical dissipation embedded in upwind schemes reduce the aliasing error?
(iii) Is it possible to estimate the effect of numerical dissipation on resolved scales?
(iv) Can we find an 'optimal' upwind scheme that balances the aliasing and finite-differencing errors such that the total error is minimized?

In addition, the investigation of the suitability of high-order accurate, centered compact difference schemes for LES of flow in complex geometries is another objective of the present study. Especially, an emphasis is taken on investigating conflicting conclusions made by [5–7,9] about the formulation of nonlinear term: one-dimensional analysis on the aliasing error and conservation property [5,6,9] suggests the use of the skew-symmetric form, while a recent *a priori* test on the isotropic turbulence [7] advocates the advective form.

The present paper is organized as follows. Section 2 introduces the finite difference schemes considered in this study. In Section 3, analyses on the static numerical errors are presented. The power spectral densities of the finite-differencing and aliasing errors and SGS forces are compared both in the continuous and discrete Fourier spaces. Section 4 deals with a dynamic error analysis by LES of an isotropic, decaying turbulence. In Section 5, the computational results of fully developed channel flow at $Re = 23000$ and flow past a circular cylinder at $Re = 3900$ are presented. A brief summary and conclusions are given in Section 6.

## 2. Finite difference schemes

As a basic finite difference scheme, we consider one parameter family of compact upwind difference [14] which is defined for any scalar $f$

$$(1+\alpha)\left.\frac{\delta f}{\delta x}\right|_{i-1} + 4\left.\frac{\delta f}{\delta x}\right|_{i} + (1-\alpha)\left.\frac{\delta f}{\delta x}\right|_{i+1} = \frac{1}{h}\{(-3-2\alpha)f_{i-1} + 4\alpha f_i + (3-2\alpha)f_{i+1}\}, \tag{1}$$

where $\delta/\delta x$ denotes a numerical approximation of the derivative, and $h = x_{i+1} - x_i$ is the grid spacing. Eq. (1) reduces to the 4th-order compact scheme [30] (denoted as COM4 hereinafter) when $\alpha = 0$. For other values of $\alpha$, (1) represents 3rd-order accurate, compact upwind-biased schemes (CUD). As Zhong [14] recommended 0.25 as a proper choice of $\alpha$, we refer to (1) with $\alpha = 0.25$ as CUDZ. If $\alpha = 1.5$, (1) corresponds to the compact upwind scheme proposed by Tolstykh and Lipavskii [15], which is referred to as CUD3 following their notation. For convenience, non-compact, standard $n$th-order accurate central and upwind schemes are denoted by CD$n$ and UD$n$, respectively.

Modified wavenumbers (MWNs) [30] for these compact schemes are plotted in Fig. 1, together with those for spectral method (SP), UD5 and UD7. It is shown that the amount of dissipation characterized by the imaginary part of MWN increases with increasing $\alpha$. Therefore, $\alpha$ can be regarded as a measure of numerical dissipation embedded in the difference scheme. Thus, one can roughly represent the spectral characteristics of most upwind schemes with (1) by controlling the parameter $\alpha$. For example, MWN of UD7 is quite similar to that of CUDZ. On the other hand, the dispersion characteristics represented by the real part of MWN also significantly changes with $\alpha$. Nevertheless, this fact can be ignored because, as will be shown in this paper, we investigate the effect of numerical dissipation in the range of $0 \leqslant \alpha \leqslant 0.25$ where the dispersion characteristics is nearly unchanged. Note also that throughout this paper, we define the numerical dissipation as the dissipation caused solely by the dissipative error from the imaginary part of MWN.

For upwind schemes ($\alpha \neq 0$), the direction of flow or wave should be taken into account. In this paper, the following local Lax–Friedrichs (LLF) flux-vector splitting (FVS) is considered

$$\mathbf{F}^{\pm}(\mathbf{Q}) = \frac{1}{2}(\mathbf{F}(\mathbf{Q}) \pm |\Lambda|\mathbf{Q}), \tag{2}$$

where $\mathbf{Q}$ is the conservative variable vector, and $|\Lambda| = \mathrm{diag}(|\lambda_1|, |\lambda_2|, \ldots)$ is the local eigenvalue matrix of flux vector $\mathbf{F}(\mathbf{Q})$. For flow over a circular cylinder (Section 5.3), we use Van Leer FVS [31] instead of LLF-FVS to avoid oscillation near the stagnation point. For negative flux of (2), a scheme that has symmetric coefficients to (1) about $x_i$ is used to get the spatial derivatives. It should be noted that we only consider the finite difference schemes defined on the regular grid where all the variables and derivatives are defined on the same node points. However, there is a class of upwind schemes that cannot be represented by (1), which are defined on the collocated grid using the nonlinear interpolation at the cell faces. Those schemes and their numerical dissipation are explained later in this paper.

For most upwind schemes, the concept of flux vector enforces the nonlinear term to be written in the conservative, or divergence form. Moreover, in the presence of shock-like flow structures, the divergence form is preferred for capturing the discontinuity without oscillation. For turbulent flow, however, this constraint may affect the simulation result because the form of nonlinear term has a significant influence on

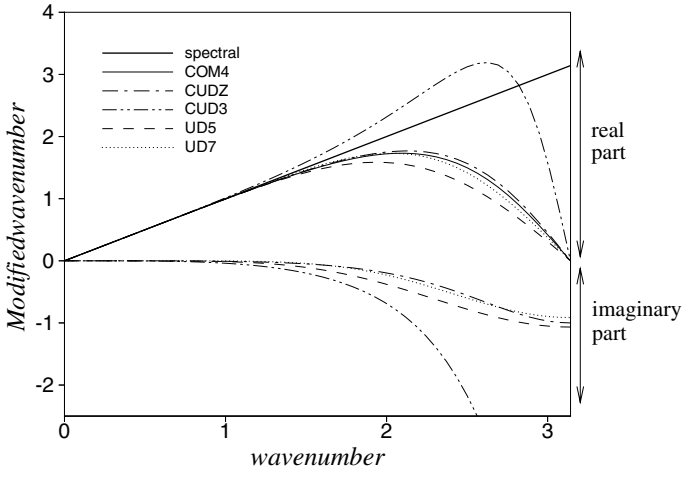


Fig. 1. Modified wavenumbers for various finite difference schemes.

the discretization error [7,9,10]. In cases of centered difference, on the other hand, we consider three analytically but not numerically equivalent forms of nonlinear term:

$$\begin{aligned} N_i^{\mathrm{d}} &= \frac{\partial(\rho u_i u_j)}{\partial x_j}, \quad \text{divergence or conservative form,} \\ N_i^{\mathrm{a}} &= \rho u_j \frac{\partial u_i}{\partial x_j} + u_i \frac{\partial \rho u_j}{\partial x_j}, \quad \text{advective or convective form,} \\ N_i^{\mathrm{s}} &= \frac{1}{2}\left(N_i^{\mathrm{d}} + N_i^{\mathrm{a}}\right), \quad \text{skew-symmetric form,} \end{aligned} \tag{3}$$

where $\rho$ is the density of fluid and $u_i$ is the velocity vector. Although the rotational form is another possible formulation that is commonly adopted in the spectral method (see, for instance [7,9]), it is not considered here because it is rarely used in the physical space simulation. For notational convenience, extensions -div, -adv and -sk will be used to specify which form of nonlinear term is used.

## 3. Static error analysis

### 3.1. Finite-differencing error, aliasing error and SGS force

Let us consider an incompressible, isotropic turbulence in a cubic box $\Omega$ of side $L$. Such isotropic turbulence obeys the following Navier–Stokes equation:

$$\frac{\partial u_i}{\partial t} = -\frac{1}{\rho} N_i - \frac{\partial P}{\partial x_i} + \nu \frac{\partial^2 u_i}{\partial x_j \, \partial x_j}, \tag{4}$$

where $u_i = (u_1, u_2, u_3)$ is the solenoidal velocity field and $N_i$ is the nonlinear term of any form in (3), $P = p/\rho$ is a scalar functional determined by the continuity condition, and $\nu$ is the kinematic viscosity.

First, the power spectral densities of static discretization errors and SGS forces are defined in the continuous Fourier space (Section 3.1.1). Then, the result is recast into the discrete wavevector space to deal with upwind schemes and various forms of the nonlinear term (Sections 3.1.2 and 3.1.3). Although important results in the continuous space were already described by Ghosal [8], we will briefly summarize them for the completeness and consistency with the present approach on the discrete domain.

#### 3.1.1. Discretization errors and SGS forces in the continuous wavevector space

The exact solution of (4) can be obtained in the wavevector space $\mathbf{k} = (k_1, k_2, k_3) \in \mathbf{R}^3$, where $k_i = 2\pi n_i / L$, $n_i$s are integers, and $L$ is assumed to be infinity to make $\mathbf{k}$ a continuous wavevector. However, we should define a 'numerically exact' solution on a finite domain to make a fair comparison with actual numerical solutions. We seek the most accurate, or ideal numerical solution of (4) that can be obtained in the continuous but confined space $B \equiv [-\pi/\Delta, \pi/\Delta]^3 \equiv [-k_m, k_m]^3$, where $\Delta$ is the grid spacing and $k_m$ is the maximum resolvable wavenumber.

The most accurate numerical solution is obtained by applying the 'exact' SGS stress to the filtered Navier–Stokes equation with the filter width $\Delta_{\mathrm{f}} = \Delta$. Therefore, the ideal solution is governed by the following equation:

$$\frac{\partial \hat{u}_i(\mathbf{k})}{\partial t} = -\mathrm{i} k_n P_{im}(\mathbf{k}) \left[ \hat{G}(\mathbf{k}) \int_B \int_B \delta(\mathbf{p} + \mathbf{q} - \mathbf{k}) \hat{u}_m(\mathbf{p}) \hat{u}_n(\mathbf{q}) \, \mathrm{d}\mathbf{p} \, \mathrm{d}\mathbf{q} + \hat{\tau}_{mn}(\mathbf{k}) \right] - \nu k^2 \hat{G}(\mathbf{k}) \hat{u}_i(\mathbf{k}), \tag{5}$$

where $\widehat{(\cdot)}$ denotes the Fourier coefficient, $\delta$ is the Dirac delta function, $\tau_{mn}$ is the SGS stress, $P_{ij}(\mathbf{k}) = \delta_{ij} - k_i k_j/k^2$ is the projection tensor [32] onto the plane perpendicular to $\mathbf{k}$, and $\hat{G}(\mathbf{k})$ is the spectral transfer function of the filter kernel $G(\mathbf{r})$. To precisely separate the resolved scale from the SGS scale, a sharp cut-off filter is used. For this filter, $\hat{G}(\mathbf{k})$ is defined as

$$\hat{G}(\mathbf{k}|k_m) = \begin{cases} 1 & \text{if } \mathbf{k} \in B = [-k_m, k_m]^3, \\ 0 & \text{otherwise.} \end{cases} \tag{6}$$

By definition, the exact SGS stress is

$$\hat{\tau}_{ij}(\mathbf{k}) = \hat{G}(\mathbf{k}) \left[ \int\int - \int_B \int_B \right] \hat{u}_i(\mathbf{p}) \hat{u}_j(\mathbf{q}) \delta(\mathbf{p} + \mathbf{q} - \mathbf{k}) \, \mathrm{d}\mathbf{p} \, \mathrm{d}\mathbf{q}, \tag{7}$$

which corresponds to $\tau_{ij} = \overline{u_i u_j} - \overline{\bar{u}_i \bar{u}_j}$ in the physical space, and the bar denotes the cut-off filter.

Now, we consider an actual numerical solution of (4) with finite difference schemes in the continuous physical space. By introducing MWNs and aliasing modes, (5) is expressed as

$$\begin{aligned} \frac{\partial \hat{u}_i(\mathbf{k})}{\partial t} = & -\mathrm{i} k'_n P'_{im}(\mathbf{k}, \mathbf{k}') \left[ \hat{G}(\mathbf{k}) \sum_{\mathbf{a} \in \Lambda} \int_B \int_B \delta(\mathbf{p} + \mathbf{q} - \mathbf{k} - \mathbf{a}) \hat{u}_m(\mathbf{p}) \hat{u}_n(\mathbf{q}) \, \mathrm{d}\mathbf{p} \, \mathrm{d}\mathbf{q} + \hat{\tau}_{mn}(\mathbf{k}) \right] \\ & - \nu k'' \hat{G}(\mathbf{k}) \hat{u}_i(\mathbf{k}), \end{aligned} \tag{8}$$

where $k'$ and $k''$ denote MWNs of first and second derivatives, respectively, and $\Lambda$ is defined as $\Lambda = (2pk_m, 2qk_m, 2rk_m)$, where $p, q, r$ may have 0, $\pm 1$. Note that the numerical biased projection tensor $P'_{ij}(\mathbf{k}, \mathbf{k}') = \delta_{ij} - k'_i k_j/(k'_l k_l)$ [7] is introduced in (8) instead of $P_{ij}(\mathbf{k}')$ [8] to insure divergence-free velocity field at machine precision even with the finite difference schemes.

The static discretization error excluding time-stepping error is defined as the difference between the right-hand sides of (5) and (8). As stated in Section 1, this error is decomposed into the finite-differencing (FD) and aliasing errors

$$\begin{aligned} E_i^{\mathrm{FD}}(\mathbf{k}) = & \mathrm{i} \hat{G}(\mathbf{k}) \left\{ k'_n P'_{im}(\mathbf{k}, \mathbf{k}') - k_n P_{im}(\mathbf{k}) \right\} \left[ \int\int \delta(\mathbf{p} + \mathbf{q} - \mathbf{k}) \hat{u}_m(\mathbf{p}) \hat{u}_n(\mathbf{q}) \, \mathrm{d}\mathbf{p} \, \mathrm{d}\mathbf{q} \right] \\ & + \nu (k'' - k^2) \hat{G}(\mathbf{k}) \hat{u}_i(\mathbf{k}), \end{aligned} \tag{9}$$

$$E_i^{\mathrm{alias}}(\mathbf{k}) = \mathrm{i} k'_n P'_{im}(\mathbf{k}, \mathbf{k}') \hat{G}(\mathbf{k}) \sum_{\mathbf{a} \in \Lambda_0} \int_B \int_B \delta(\mathbf{p} + \mathbf{q} - \mathbf{k} - \mathbf{a}) \hat{u}_m(\mathbf{p}) \hat{u}_n(\mathbf{q}) \, \mathrm{d}\mathbf{p} \, \mathrm{d}\mathbf{q}, \tag{10}$$

where $\Lambda_0 = \Lambda - \{0, 0, 0\}$. The statistics of these errors are characterized by their power spectral density (PSD). Using the 'joint-normal approximation' [32] (see [8] for more details), PSD of the finite-differencing error is obtained as

$$\begin{aligned} \mathscr{E}^{\mathrm{FD}}(k) \equiv & 4\pi k^2 \lim_{L \to \infty} \frac{8\pi^3}{L^3} \left\{ E_i^{\mathrm{FD}}(\mathbf{k}) E_i^{\mathrm{FD}*}(\mathbf{k}) \right\}_\Omega \\ = & \left\{ 8\pi k^2 \Delta_{imn}(\mathbf{k}, \mathbf{k}') \Delta^*_{ipq}(\mathbf{k}, \mathbf{k}') \int \Phi^*_{mp}(\mathbf{r}) \Phi^*_{nq}(\mathbf{k} - \mathbf{r}) \, \mathrm{d}\mathbf{r} + 4\pi k^2 \nu^2 \left| k'' - k^2 \right|^2 \Phi_{ii}(\mathbf{k}) \right\}_\Omega, \end{aligned} \tag{11}$$

where $\{ \}_\Omega$ denotes the spherical average at radius $k = |\mathbf{k}|$, superscript * denotes the complex conjugate, and $\Delta_{imn}(\mathbf{k}, \mathbf{k}') \equiv k'_n P'_{im}(\mathbf{k}, \mathbf{k}') - k_n P_{im}(\mathbf{k})$. $\Phi_{ij}(\mathbf{k})$ is the velocity correlation tensor of the isotropic turbulence given by

$$\Phi_{ij}(\mathbf{k}) = \frac{E(k)}{4\pi k^2}(k^2\delta_{ij} - k_i k_j), \tag{12}$$

where $E(k)$ is the prescribed three-dimensional energy spectrum. Note that PSD of the finite-differencing error can be obtained from MWN of the finite difference scheme and the prescribed energy spectrum.

PSD of the aliasing error can be computed similarly as

$$\mathscr{E}^{\text{alias}}(k) = 8\pi k^2 \sum_{\mathbf{a}\in\Lambda_0} \left\{ k_n P'_{im}(\mathbf{k},\mathbf{k}')(k_q P_{ip}(\mathbf{k},\mathbf{k}'))^* \int_B \int_B \Phi^*_{mp}(\mathbf{r})\Phi^*_{nq}(\mathbf{s})\delta(\mathbf{k}+\mathbf{a}-\mathbf{r}-\mathbf{s})\,\mathrm{d}\mathbf{r}\,\mathrm{d}\mathbf{s} \right\}_\Omega. \tag{13}$$

However, PSD of the aliasing error cannot be computed analytically because (13) contains an integration inside a box which breaks the spherical symmetry. Instead, lower and upper bounds are defined in the domains $\mathscr{S}_1$ and $\mathscr{S}_2$, respectively, where $\mathscr{S}_1$ denotes the largest sphere in $B$ and $\mathscr{S}_2$ denotes the smallest sphere that contains $B$.

From (7), PSD of the SGS force is defined as follows:

$$\mathfrak{I}(k) = 4\pi k^2 \lim_{L\to\infty} \frac{8\pi^2}{L^3} \left\{ F_i^{>}(\mathbf{k}) F_i^{>*}(\mathbf{k}) \right\}_\Omega, \tag{14}$$

$$F_i^{>}(\mathbf{k}) = -\mathrm{i}k_n P_{im}(\mathbf{k})\hat{\tau}_{mn}(\mathbf{k}) = -\mathrm{i}k_n P_{im}(\mathbf{k})\hat{G}(\mathbf{k}) \left[ \int\int - \int_B \int_B \right] \hat{u}_m(\mathbf{p})\hat{u}_n(\mathbf{q})\delta(\mathbf{p}+\mathbf{q}-\mathbf{k})\,\mathrm{d}\mathbf{p}\,\mathrm{d}\mathbf{q}. \tag{15}$$

As (15) also contains the integration over $B$, the evaluation of (15) should be replaced by integrations over $\mathscr{S}_1$ (upper bound) and $\mathscr{S}_2$ (lower bound), respectively.

*3.1.2. Discrete evaluation of numerical errors*

We showed in Section 3.1.1 that PSDs of the discretization errors and SGS force can be evaluated analytically from (11), (13) and (14) once the energy spectrum and the MWN of the scheme are given. However, it is true only for central difference schemes. As upwind schemes require the information on the flow direction at each point, we need a complete velocity field rather than its spectrum. Moreover, the velocity field should be defined on the discrete wavevector space, as it is nearly impossible to prescribe the velocity field of the isotropic turbulence in the continuous wavevector space.

Therefore, the discretization errors described in Section 3.1.1 are defined in the discrete wavevector space. For this purpose, it is convenient to consider these errors first in the continuous physical space and then convert them to the discrete Fourier space.

Let us define $e_i^{\text{FD}}(\mathbf{x})$ as the finite-differencing error (9) in the physical space. It can be written as

$$e_i^{\text{FD}}(\mathbf{x}) = \mathscr{P}\left[ \left( -\frac{\partial}{\partial x_j} + \frac{\delta}{\delta x_j} \right) \left( \overline{\overline{u}_i \overline{u}_j} + \overline{P}\delta_{ij} + \tau_{ij} \right) \right] + \nu \left( \frac{\partial^2}{\partial x_j\,\partial x_j} - \frac{\delta^2}{\delta x_j\,\delta x_j} \right) \overline{u}_i, \tag{16}$$

where $\mathscr{P}$ denotes the projection onto the solenoidal field and the commutation between the filter and the derivative is assumed. Note that $e_i^{\text{FD}}(\mathbf{x})$ is defined in the continuous $\mathbf{x} \in \mathbf{R}^3$ although it does not have smaller scale than $\Delta$.

As described in Section 2, FVS is applied to nonlinear term. For example, the derivative of flux vector $\mathbf{F}(\mathbf{u})$ is given by

$$\frac{\delta \mathbf{F}(\mathbf{u})}{\delta x} = \frac{\delta^+ \mathbf{F}^+(\mathbf{u})}{\delta x} + \frac{\delta^- \mathbf{F}^-(\mathbf{u})}{\delta x}, \tag{17}$$

where the operators $\delta^+/\delta x$ and $\delta^-/\delta x$ denote upwind and downwind schemes, respectively, which are symmetric to each other. Using MWN, (17) is converted to the Fourier space as

$$\widehat{\frac{\delta \mathbf{F}(\mathbf{u})}{\delta x}} = \mathrm{i}k'_x \widehat{\mathbf{F}^+(\mathbf{u})} + \mathrm{i}k'^*_x \widehat{\mathbf{F}^-(\mathbf{u})}, \tag{18}$$

where $k'^*_x$ is the complex conjugate of MWN in the $x$-direction. Using (18), the projection of (16) onto the discrete Fourier domain $B_N \equiv [-N/2, N/2]^3 = [-k_M, k_M]^3$ takes the form of

$$\begin{aligned} E_i^{\mathrm{FD}}(\mathbf{k}|k_M) = \hat{G}(\mathbf{k}|k_M)\Big[&\Big\{P'_{im}(\mathbf{k},\mathbf{k}')\hat{N}'_m(\mathbf{k}') - P_{im}(\mathbf{k})\hat{N}_m(\mathbf{k})\Big\} \\ &+ \mathrm{i}\hat{\tau}_{mn}(\mathbf{k})\Big\{k'_n P'_{im}(\mathbf{k},\mathbf{k}') - k_n P_{im}(\mathbf{k})\Big\} + \nu(k'' - k^2)\hat{u}_i(\mathbf{k})\Big], \end{aligned} \tag{19}$$

and

$$\hat{N}_m(\mathbf{k}) = \mathrm{i}k_n \sum_{\mathbf{p}+\mathbf{q}=\mathbf{k}} \hat{u}_m(\mathbf{p})\hat{u}_n(\mathbf{q}), \tag{20}$$

$$\hat{N}'_m(\mathbf{k}') = \mathrm{i}k'_n \widehat{C^+_{mn}} + \mathrm{i}k'^*_n \widehat{C^-_{mn}}, \quad C^{\pm}_{mn} = \frac{1}{2}\left(u^M_m \pm |u^M_m|\right)u^M_n, \tag{21}$$

where $k_M$ corresponds to the smallest scale $\Delta$. In (21), $u^M_m$ is the inverse discrete Fourier transform of $\hat{u}_m(\mathbf{k})$ with modes up to $M = (3/2)N$ in each direction, i.e.,

$$u^M_m = I^3_M u_m(\mathbf{x}) = \sum_{\mathbf{k}} \tilde{u}_m(\mathbf{k})\mathrm{e}^{\mathrm{i}\mathbf{k}\cdot\mathbf{x}}, \tag{22}$$

where

$$\tilde{u}_m(\mathbf{k}) = \begin{cases} \hat{u}_m(\mathbf{k}) & \text{if } \mathbf{k} \in B_N, \\ 0 & \text{otherwise} \end{cases} \tag{23}$$

and

$$\mathbf{x} = x_i\mathbf{e}_i = \frac{n_i L}{M}\mathbf{e}_i, \quad n_i = 0, \ldots, M-1,$$

$$\mathbf{k} = k_i\mathbf{e}_i = \frac{2\pi l_i}{L}\mathbf{e}_i, \quad l_i = -M/2, \ldots, M/2-1$$

for orthonormal basis $(\mathbf{e}_1, \mathbf{e}_2, \mathbf{e}_3)$ and $i = 1, 2, 3$. Without loss of generality, we assume $L = 2\pi$ as we deal with a discrete and finite domain both in the physical and Fourier spaces. Eqs. (22) and (23) are the so called 3/2-rule, or zero padding technique [33], which are introduced to remove the aliasing error. In the evaluation of (19), the error from viscous term is neglected because it is very small for most flows [8]. The discrete evaluation of SGS stress term in (19) will be given in Section 3.1.3.

Although the discrete evaluation is an inevitable choice to deal with upwind schemes, it has some advantages over continuous one. One of them is that the aliasing error can be evaluated efficiently and uniquely, which is simply computed by the difference between dealiased and aliased numerical evaluations of nonlinear term

$$E_i^{\mathrm{alias}}(\mathbf{k}|k_M) = -\hat{G}(\mathbf{k})P'_{im}(\mathbf{k},\mathbf{k}')\Big\{\hat{N}'^{DA}_m(\mathbf{k}') - \hat{N}'^{\mathrm{alias}}_m(\mathbf{k}')\Big\}, \tag{24}$$

where $\hat{N}_m'^{DA}(\mathbf{k}')$ denotes the dealiased nonlinear term as defined in (21) and $\hat{N}_m'^{\text{alias}}(\mathbf{k}')$ is the aliased one that can be also obtained from (21) by simply replacing $M$ with $N$. The computation of (24) is much easier than that of (10), in that (10) requires the evaluation of three (1-D, 2-D and 3-D) different aliasing modes [8].

Another advantage of the discrete approach is that different forms of nonlinear term can be easily computed for the case of centered difference schemes. For example, the finite-differencing and aliasing errors for the advective and skew-symmetric forms (see (3)) are obtained by the modification of $\hat{N}_m'(\mathbf{k}')$ (and $\hat{N}_m(\mathbf{k})$) in (19) and (24) such as

$$\hat{N}_m'(\mathbf{k}')^a = \mathrm{i}\sum_{\mathbf{p}+\mathbf{q}=\mathbf{k}} \left(p_n' + q_n'\right)\hat{u}_m(\mathbf{p})\hat{u}_n(\mathbf{q}), \tag{25}$$

$$\hat{N}_m'(\mathbf{k}')^{\mathrm{s}} = \frac{1}{2}\mathrm{i}k_n' \sum_{\mathbf{p}+\mathbf{q}=\mathbf{k}} \hat{u}_m(\mathbf{p})\hat{u}_n(\mathbf{q}) + \frac{1}{2}\mathrm{i}\sum_{\mathbf{p}+\mathbf{q}=\mathbf{k}} \left(p_n' + q_n'\right)\hat{u}_m(\mathbf{p})\hat{u}_n(\mathbf{q}). \tag{26}$$

In the continuous approach [8], however, only the divergence form is considered possibly due to some analytical complexity in dealing with other forms of nonlinear term. Note that the discretization errors, (19) and (24), are derived directly from the prescribed velocity field without resort to the joint-normal hypothesis.

### 3.1.3. Velocity field and SGS force

Two models are considered for the energy spectrum in the present study: the Von Karman spectrum $E^{\text{high}}$ and the conventional Gaussian model $E^{\text{low}}$ of the isotropic turbulence, which are given, respectively, as

$$E^{\text{high}}(k) = \frac{a\left(k/k_p\right)^4}{\left\{b + \left(k/k_p\right)^2\right\}^{17/6}}, \tag{27}$$

$$E^{\text{low}}(k) = c\left(k/k_p\right)^4 \exp\left\{-2\left(k/k_p\right)^2\right\}, \tag{28}$$

where $a = 2.683$, $b = 0.417$ and $c = 7.389$. The spectra ($E^{\text{high}}$ and $E^{\text{low}}$) representing high and low Reynolds number flows, respectively, are normalized such that the maximum energy is 1 at $k = k_p$. Since we are more interested in the high Reynolds number flow, all the results in this section are from the Von Karman spectrum unless otherwise specified.

Although the 'phase jittering' technique [7] is often used to generate a realistic random velocity field, the non-Gaussian nature of real turbulent flow [34] is not produced by such a synthetic field. As an alternative, an iterative method proposed by Carati et al. [35] is adopted to generate a field that satisfies the continuity, prescribed energy spectra and realistic velocity-derivative skewness close to −0.5. Fig. 2 shows prescribed and recovered 3-D energy spectra for the Von Karman and Gaussian models. It is shown that the prescribed spectra are well recovered by the present method.

For the purpose of validation, we compare the present results on the discrete wavevector space with those from Ghosal [8] for the case of $k_M = 8$, where the Von Karman model (27) with $k_p = 1$ is used. Unlike [8], the same values $k_M$ and $k_p$, however, cannot be used for the present study since we deal with only integer wavenumbers: $k_p = 1$ and integer wavenumbers up to $k_M = 8$ are insufficient even for representing the Von Karman spectrum. In order to make an appropriate comparison with the results on the continuous space, we set $k_p = 4$ and $k_M = 32$. Finally, the computed discretization error and SGS force are rescaled such that the results on 32 equi-spaced spherical shells can be a good approximation of those in the continuous three-dimensional wavenumber $k$ ($0 \leqslant k \leqslant 8$). Thus, integer-valued wavenumbers in this subsection do not cor-

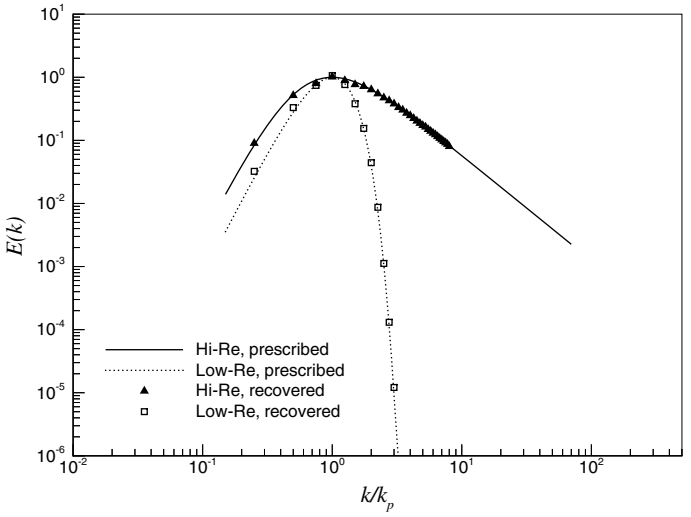


Fig. 2. Prescribed and recovered energy spectra for high Reynolds number (Von Karman) and low Reynolds number (Gaussian) models.

respond to discrete grid points in the physical space. Instead, they are interpreted as the discrete approximations of discretization errors and SGS force that were originally defined in the continuous space.

Now, let us consider the discrete evaluation of SGS stress, (7). However, as there is no mode outside $B_N$, it cannot be directly approximated with the discrete velocity field. Therefore, we consider a new velocity field ($u_j^{2N}$) generated from twice the grid points in each direction. Then, SGS stress is approximated by

$$\tau_{ij} = \overline{u_i u_j} - \overline{\overline{u}_i \overline{u}_j} \approx \overline{u_i^{2N} u_j^{2N}} - \overline{u_i^N u_j^N}, \tag{29}$$

where $u_j^N$ is the original velocity field in $B_N$. A justification for this approximation is that the nonlinear dynamics of the resolved modes with wavenumbers $k < k_c = k_M$ are governed almost exclusively by their interactions with a limited range of modes with wavenumbers not exceeding $2k_c$, and much smaller scales have a negligible effect on the resolved ones [4]. Eq. (29) is represented in the Fourier space as

$$\hat{\tau}_{ij}(\mathbf{k}) = \hat{G}(\mathbf{k}|k_M)\left( \sum_{\mathbf{p}+\mathbf{q}=\mathbf{k}}^{p,q,k \leqslant 2k_M} \hat{u}_i^{2N}(\mathbf{p})\hat{u}_j^{2N}(\mathbf{q}) - \sum_{\mathbf{p}+\mathbf{q}=\mathbf{k}}^{p,q,k \leqslant k_M} \hat{u}_i^{N}(\mathbf{p})\hat{u}_j^{N}(\mathbf{q}) \right). \tag{30}$$

In practice, we first generate $u_j^{2N}$ on $(2N)^3$ grids and obtain $u_j^N$ by filtering $u_j^{2N}$ at $k_M$ to insure that $u_j^{2N}$ has the same spectral information with $u_j^N$ up to $k_M$. Finally, PSD of the SGS force is obtained by (14) and (15).

Fig. 3 shows PSDs of SGS forces (14) computed from the continuous wavevector approach (Eq. (7) and [8]) and the present discrete evaluation (Eq. (30)). Also shown is the spectrum of total nonlinear term, which can be easily obtained by replacing $\Delta_{imn}(\mathbf{k}, \mathbf{k}')$ in (11) with $-k_n P_{im}(\mathbf{k})$. It is shown that the discrete true SGS force lies between the lower and upper bounds of the SGS force computed from the continuous evaluation except the high wavenumber region near the cut-off. Therefore, we can regard this discrete SGS force as the reference 'true SGS force'.

Although the main concern of this paper is on the discretization error, the modelling error from the empirical SGS models should be investigated. This issue is addressed in Appendix A.

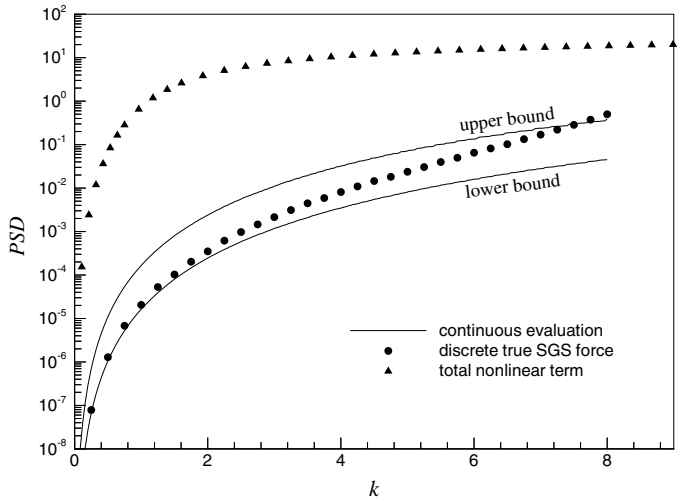


Fig. 3. Power spectra of SGS forces.

### 3.2. Analysis on discretization errors

Figs. 4(a) and (b) show PSDs of the finite-differencing errors of UD1, CD2-div, UD5, CD6-div, CUD3, CUDZ, and COM4-div evaluated by the discrete method described in Section 3.1.2, together with PSD of the SGS force. Also shown in Fig. 4 are PSDs by the continuous evaluation (see Section 3.1.1 and [8]) for CD2-div, CD6-div and COM4-div for the validation of the present discrete evaluation. The comparison of the spectra between the discrete and continuous evaluations indicates that the finite-differencing errors are accurately produced by the present discrete approach.

It is shown in Fig. 4 that in general high-order schemes have lower finite-differencing errors and upwind schemes have larger errors than corresponding central difference schemes. Especially, errors from UD1 are much larger than the SGS force, demonstrating that such a scheme should not be used in LES at all. The comparison between compact and non-compact difference schemes demonstrates the superiority of com-

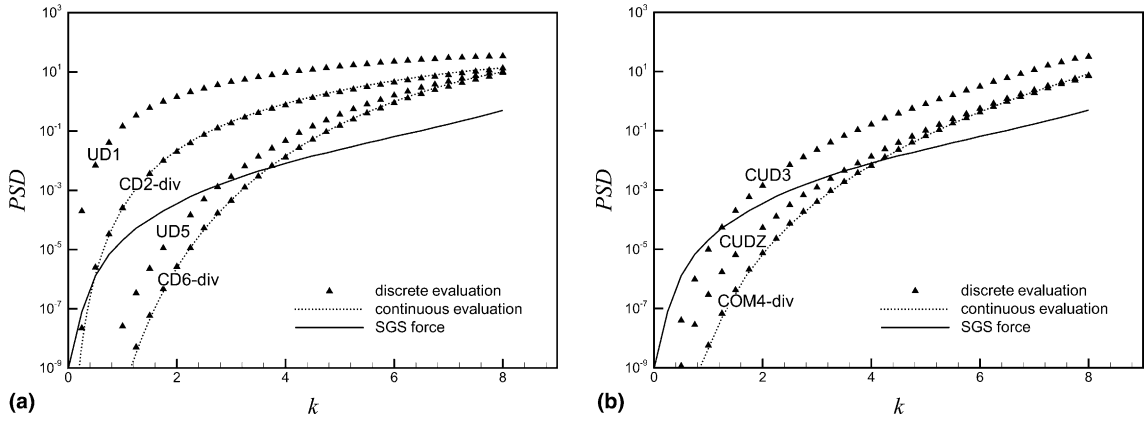


Fig. 4. Finite-differencing errors for various schemes as compared with the SGS force: (a) UD1, CD2-div, UD5 and CD6-div; (b) CUD3, CUDZ and COM4-div.

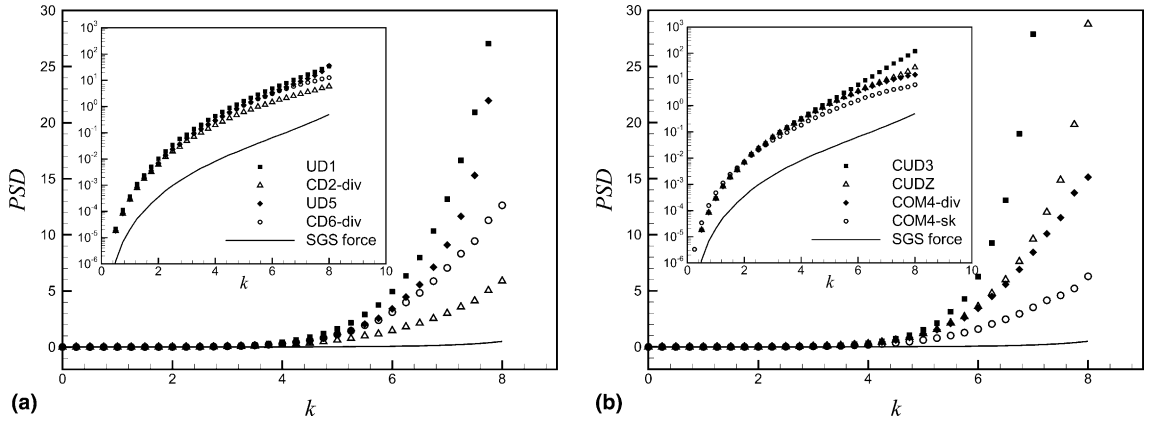


Fig. 5. Aliasing errors for various schemes as compared with the SGS force: (a) UD1, CD2-div, UD5 and CD6-div; (b) CUD3, CUDZ, COM4-div and COM4-sk.

pact schemes over non-compact ones of comparable order of accuracy. This result is consistent with the modified wavenumber analysis.

Fig. 5(a) shows PSDs of the aliasing errors of UD1, CD2-div, UD5 and CD6-div both in log and real scales. Also shown in Fig. 5(b) are those of CUD3, CUDZ, COM4-div and COM4-sk. Unlike the finite-differencing errors, the aliasing errors are much larger than the SGS force regardless of the discretization schemes, indicating that the aliasing errors are the dominant source of discretization error even for low-order schemes.

For central differences, it is manifest that higher-order schemes have higher aliasing errors [8]. However, for upwind schemes, the aliasing error is shown to be nearly proportional to the imaginary part of MWN: The more dissipative is the scheme, the larger aliasing error is obtained, contrary to the common belief on upwind schemes. The aliasing errors of UD1 and CUD3 are larger than those of UD5 and CUDZ, respectively. Moreover, aliasing errors of upwind schemes are larger than those of comparable central schemes. This result seems to give negative answers to the questions (ii) and (iv) described in Section 1,

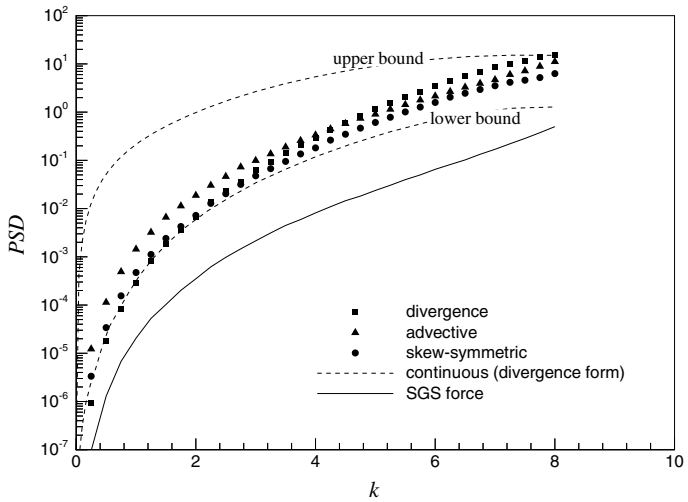


Fig. 6. Comparison of aliasing errors for different forms of nonlinear term with COM4.

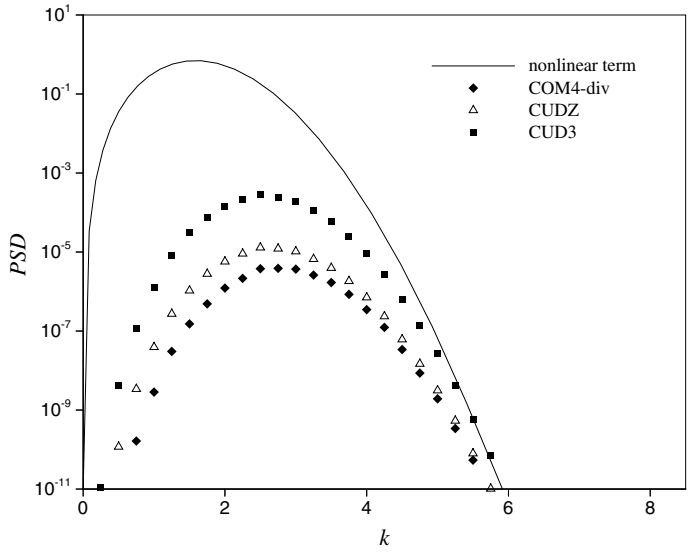


Fig. 7. Finite differencing errors with the low Reynolds number model.

because both the finite-differencing and aliasing errors increase as the numerical dissipation increases (see Appendix B for one-dimensional analysis). However, this conclusion is quite questionable because it is purely drawn from the static error analysis. Therefore, we do not draw any conclusion on this issue until the dynamic error analysis is conducted in Section 4.

Fig. 6 shows the aliasing errors of COM4 from different forms of nonlinear term. Also plotted in this figure are the lower and upper bounds of aliasing error from COM4-div evaluated by the continuous approach. It is shown that the skew-symmetric form exhibits the lowest aliasing error. Although this fact was already shown in [5,6,9] with one-dimensional analysis, Fig. 6 presents the first result with the Navier–Stokes equation. It is interesting to note that the advective form shows larger errors at low wavenumbers than the divergence form. It should be noted that even the lowest aliasing error produced by COM4-sk is still much larger than the SGS force.

On the other hand, for the low Reynolds number spectrum model (28), the SGS force as well as the aliasing error goes to machine zero at all wavenumbers, indicating that all the energetic wavenumbers are resolved with the given grid. For this case, LES becomes DNS. However, even for this case, the finite-differencing errors still exist and their PSDs are compared to that of total nonlinear term in Fig. 7. From this figure, the finite-differencing error of COM4-div is much smaller than total nonlinear term, and those from CUDZ and CUD3 are not big, which illustrates the success of upwind schemes in laminar flow simulation and well-resolved direct simulation of turbulent flow over years.

## 4. Dynamic error analysis

The static error analysis in Section 3 provides a useful information about estimating the amounts of error produced by various finite difference schemes. However, the spectral changes in time according to numerical schemes cannot be taken into account by the static error analysis. Therefore, in this section, we present a dynamic analysis on the discretization errors by simulating the decaying isotropic turbulence investigated by Comte-Bellot and Corrsin [36] (denoted as CBC hereinafter). They measured the energy

spectra at three locations in grid turbulence. Using the Taylor hypothesis, the spectra are converted to those at $tU_0/M = 42$, 98 and 171, where $M$ ($=5.08$ cm) and $U_0$ ($=10$ m/s) are the grid size and free-stream velocity, respectively. The Taylor micro-scale Reynolds numbers, $Re_\lambda$, are in the range of 71.6–60.6. The discretization errors are now estimated from the numerical solutions, not from the error terms.

The initial field is generated iteratively, as described in Section 3, to match the measured spectrum at $tU_0/M = 42$. A pseudo-spectral code is used for the simulation by adopting MWNs to mimic the physical space behavior of the finite difference schemes. All the simulations in this section are performed with a $32^3$ grid in the computational box of $(11M)^3$, but in Section 4.4, a $64^3$ grid is used to see the effect of the resolution. A third-order Runge–Kutta scheme and the Crank–Nicolson scheme are used for temporal integration of nonlinear and diffusion terms, respectively.

For the SGS model, both the spectral eddy viscosity model (SPEVM) [37] and dynamic Smagorinsky model (DSM) [2,38] are used, which are described in Appendix A.

### 4.1. Reference LES solution

Fig. 8 shows the time evolution of $E(k)$ and the decay of the resolved kinetic energy for dealiased spectral method (SPDA) with and without SGS model. The results from both SGS models agree very well with the experimental data of CBC. On the other hand, the simulation without SGS model results in large energy accumulation at high wavenumbers and hence fails to reproduce the correct decay rate of the kinetic energy. This result is natural because the resolved dissipation rate, $\epsilon = 2\nu \int_0^{k_c} k^2 E(k)\, \mathrm{d}k$, at $tU_0/M = 42$ is only 2.5% of the total dissipation rate and thus most dissipation should be supplied by the SGS dissipation.

Hence, we define the result from SPDA with SPEVM as a reference solution to study the dynamic errors. All the simulations in the following subsections adopt SPEVM because of its efficiency in the Fourier space. One could obtain essentially the same results from SM (or DSM) at least for this isotropic turbulence.

### 4.2. Effect of discretization error

Figs. 9(a)–(d) show the energy spectra at $tU_0/M = 98$ for SP (spectral), COM4, CUDZ and CUD3 with and without aliasing error. Three different forms of nonlinear term are considered for central schemes (Figs. 9(a)–(c)) and the divergence form is considered for upwind schemes (Fig. 9(d)). The comparison between

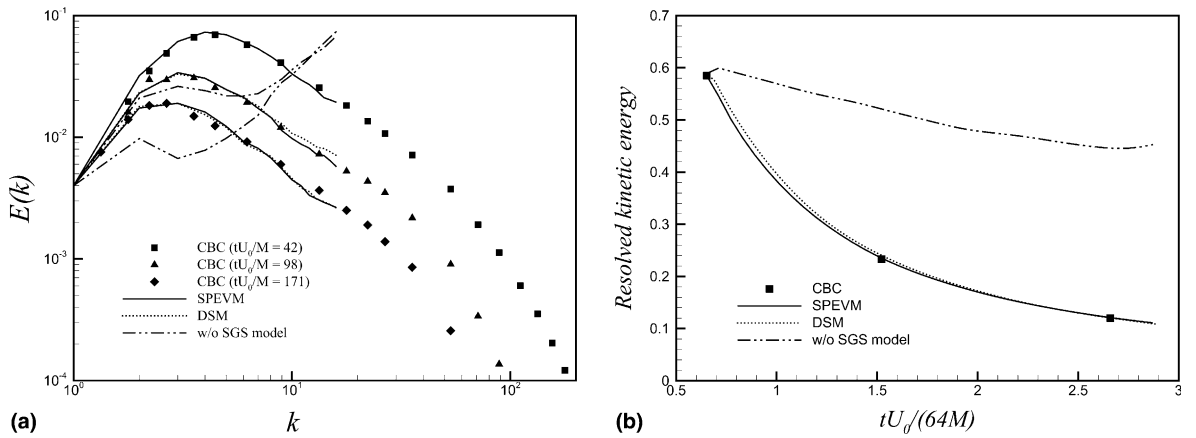


Fig. 8. Results from simulation of the decaying isotropic turbulence with and without SGS model. Computations are performed with the dealiased spectral method: (a) time evolution of energy spectra; (b) decay of the resolved kinetic energy.

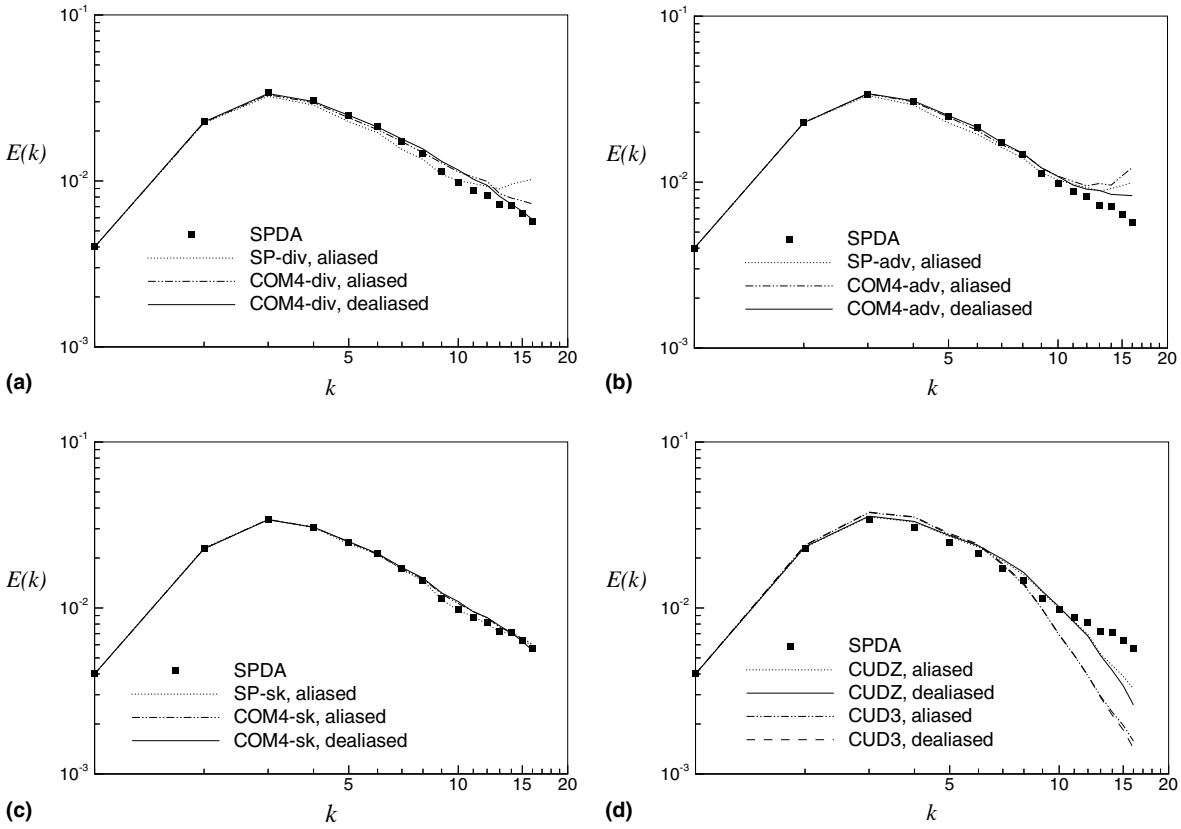


Fig. 9. Energy spectra at $tU_0/M = 98$ for various schemes with and without aliasing error: (a) spectral and COM4 in divergence form; (b) spectral and COM4 in advective form; (c) spectral and COM4 in skew-symmetric form; (d) CUDZ and CUD3 in divergence form.

results from SPDA and dealiased simulation with finite difference schemes reveals the effect of the finite-differencing error, and the comparison between aliased and dealiased simulations shows the effect of the aliasing error.

Although the finite-differencing errors are not same for different forms of nonlinear term (see Appendix B and [9]), this fact is often overlooked. From Fig. 9, it is manifest that the skew-symmetric form minimizes both the finite-differencing and aliasing errors. Thus, the success of COM4 in the skew-symmetric form comes from reduced finite-differencing error as well as reduced aliasing error. It is interesting to observe that COM4 in the advective form produces largest finite-differencing and aliasing errors. Therefore, no evidence is found from the present analysis and simulation that support the result from Fedoiun et al. [7].

On the other hand, the aliasing errors from SP in the divergence and advective forms are larger than those from COM4, whereas the spectrum from SP in the skew-symmetric form is nearly the same as that from SPDA, which suggests the use of the pseudo-spectral method in the skew-symmetric form rather than using an expensive zero padding technique in other forms of nonlinear term.

Parallel to error-minimizing characteristics, the superiority of the skew-symmetric form over other forms lies in the fact that the kinetic energy is conserved in the skew-symmetric form even in the presence of the finite-differencing and aliasing errors [9]. In general, such a conservation property is crucial for the stability of simulations that need long time integration. This issue will be addressed in the physical space simulation in Section 5.

Contrary to the static analysis, the aliasing error is smaller than the finite-differencing error and contaminates only high wavenumber regions. This is true especially for upwind schemes. For CUDZ and CUD3 (Fig. 9(d)), the dissipative finite-differencing error is the dominant source of the discretization error. Furthermore, the aliasing error of CUD3 is smaller than that of CUDZ, indicating that the aliasing error decreases as the numerical dissipation increases, which is opposite to the result obtained from the static analysis.

Possible explanations for this opposite result on the aliasing error may be given in the below. First, the interaction between the aliasing error and dissipative finite-differencing error should be considered for upwind schemes. Unlike the static analysis where the energy spectrum is fixed as a prescribed one, the energy spectrum continuously changes in time and is contaminated by the finite-differencing error leading to fall-off at high wavenumbers. For highly dissipative schemes, the finite-differencing error may leave no energy at high wavenumbers to be aliased. This mechanism explains why the aliasing error decreases as the imaginary part of MWN increases. Second, the discrepancy between the static and dynamic analyses for both central and upwind schemes can be explained in terms of the self-adjusting mechanism of SGS model by which the effect of the discretization error is reduced. This feature will be explained in the following section.

It is worth noting that the imaginary part of MWN is not the only source of numerical dissipation for upwind schemes. Appendix C deals with flux vector splitting and shock-capturing schemes as additional sources of numerical dissipation. However, it is shown by performing MILES with the present upwind schemes that such an excessive dissipation does not remove the necessity of SGS model in LES (see Appendix D).

### 4.3. Dynamic interaction between the numerical error and SGS force

We conjecture that the SGS models considered in this study have a self-adjusting mechanism in which the numerical error is considerably reduced. This may be illustrated by performing an 'ideal LES' where the SGS force is independently given as that obtained from LES with SPDA. Therefore, the difference between the actual LES and the ideal LES may show the effect of dynamic interaction between the numerical error and SGS model.

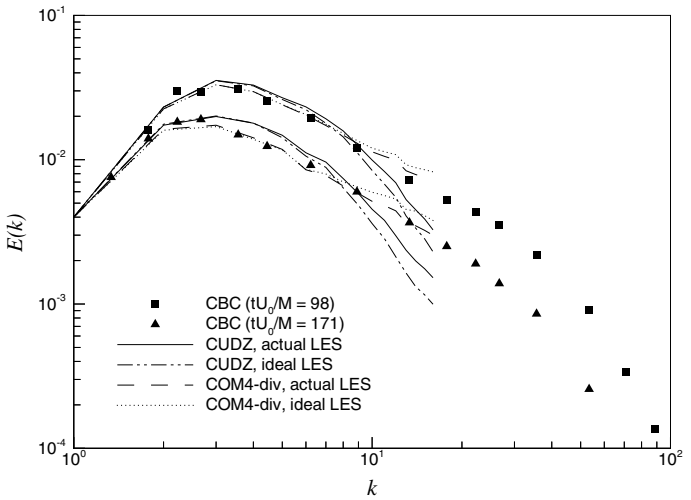


Fig. 10. Time evolutions of energy spectra from the actual LES and the ideal LES.

Fig. 10 shows the time evolutions of the energy spectra from the ideal and actual LES with COM4-div and CUDZ. For both difference schemes, it is evident that the actual LES shows better agreement with the experiment. For COM4, the effect of the aliasing error is reduced by the actual LES as the aliasing error leads to increase in the eddy viscosity at high wavenumbers through the increase in $E(k_c)$. Similarly, for CUDZ, the effect of the dissipative finite-differencing error is reduced by the actual LES because the dissipative finite-differencing error reduces the eddy viscosity through the decrease in $E(k_c)$. Note that a similar mechanism also holds for DSM [39] through the dynamic constant(s).

Therefore, in actual simulations the effect of numerical error is always smaller than what is expected from the static analysis due to the self-adjusting mechanism of SGS models.

### 4.4. Optimal upwind scheme

As shown in Section 4.2, the aliasing error decreases as the numerical dissipation increases. This suggests that there may exist some range of $\alpha$ for CUD of minimizing the total discretization error. In this subsection, such an optimal $\alpha$, *i.e.* an optimal amount of numerical dissipation, is sought from the temporal evolution of numerical errors.

We define the dynamic finite-differencing, aliasing and total errors as the differences between the solutions with and without discretization errors normalized by the total kinetic energy:

$$\begin{aligned}
\epsilon^{\mathrm{FD}}(t) &= \frac{\int_0^{k_m} |E^{\mathrm{SPDA}}(k,t) - E^{\mathrm{DA}}(k,t)|\,\mathrm{d}k}{\int_0^{k_m} E^{\mathrm{SPDA}}(k,t)\,\mathrm{d}k},\\
\epsilon^{\mathrm{alias}}(t) &= \frac{\int_0^{k_m} \left|E^{\mathrm{DA}}(k,t) - E^{\mathrm{alias}}(k,t)\right|\mathrm{d}k}{\int_0^{k_m} E^{\mathrm{SPDA}}(k,t)\,\mathrm{d}k},\\
\epsilon^{\mathrm{total}}(t) &= \frac{\int_0^{k_m} \left|E^{\mathrm{SPDA}}(k,t) - E^{\mathrm{alias}}(k,t)\right|\mathrm{d}k}{\int_0^{k_m} E^{\mathrm{SPDA}}(k,t)\,\mathrm{d}k},
\end{aligned} \tag{31}$$

where the superscript 'SPDA' means the dealiased spectral simulation, 'DA' denotes the dealiased simulation with the finite difference scheme and 'alias' denotes the aliased simulation with the finite difference scheme.

Figs. 11(a) and (b) show the time evolutions of the dynamic finite-differencing and aliasing errors for a family of compact upwind scheme with various $\alpha$. The range of $\alpha$ considered is from 0 to 0.25 that correspond to COM4-div and CUDZ, respectively. The results from COM4-sk are also plotted for comparison. The dynamic finite-differencing error increases as $\alpha$ increases, although the trend is not monotonic, whereas the dynamic aliasing error decreases monotonically with increasing $\alpha$. The aliasing error for COM4-sk is smaller than that for CUDZ ($\alpha = 0.25$).

Fig. 12(a) shows the dynamic errors as a function of $\alpha$ at three nondimensional times, where the existence of the optimal amount of dissipation is clearly observed as a consequence of different behaviors of the finite-differencing and aliasing errors. The increase in the finite-differencing error is more dominant characteristics of upwind scheme than the decrease in the aliasing error. It is also interesting to note that the finite-differencing error is even larger than the total error except for small $\alpha$: the finite-differencing error significantly decreases the kinetic energy, while the aliasing error increases it. Thus, their net effect (total discretization error) is smaller than the finite-differencing error alone.

In Fig. 12(a), $\alpha = 0.07$ is an optimum value. Hence, we call CUD with $\alpha = 0.07$ as the 'optimal CUD'. As expected, the result from optimal CUD shows an excellent agreement with SPDA and experiment (Fig. 13). Note that the optimal CUD provides a very small dissipation as comared to other popular upwind schemes,

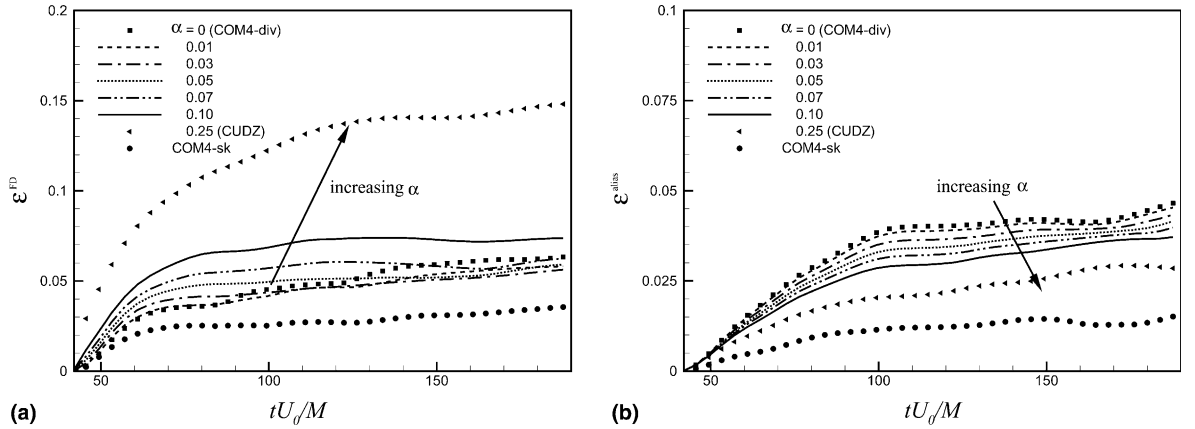


Fig. 11. Time evolutions of the dynamic errors for a family of compact upwind scheme: (a) dynamic finite-differencing error; (b) dynamic aliasing error.

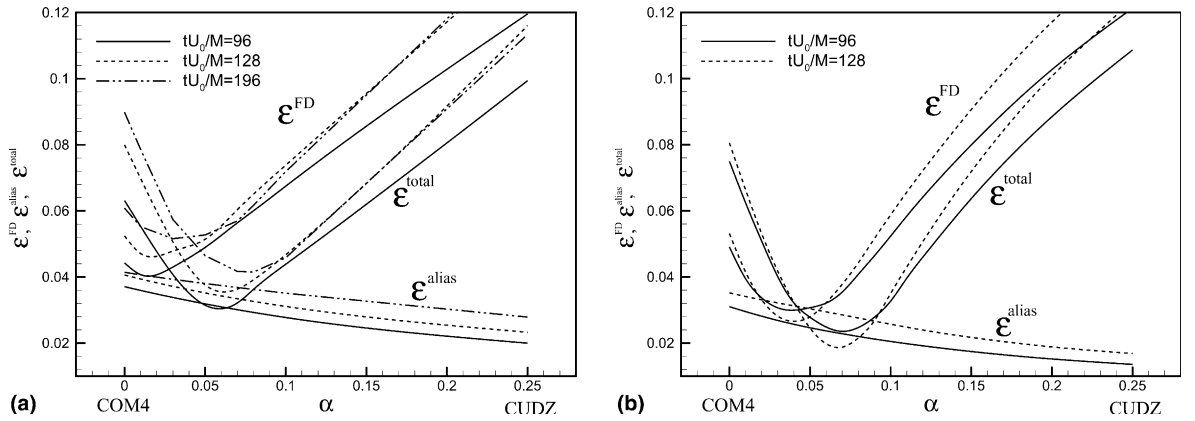


Fig. 12. Dynamic finite-differencing, aliasing and total errors as a function of $\alpha$: (a) $32^3$ simulation; (b) $64^3$ simulation.

which illustrates the failure of conventional upwind schemes because the advantage of reducing the aliasing error by upwind schemes is completely masked by the increased finite-differencing error.

To investigate the effect of grid resolution on the optimal dissipation, the dynamic errors are evaluated from the simulations with $64^3$ grids (Fig. 12(b)). The optimal $\alpha$ is nearly unchanged with the increase in the resolution. This result is encouraging but it may be simply due to the nature of the isotropic turbulence, or the strong scale-similarity of the inertial range dynamics. In general, there is no reason to believe that the optimal amount of dissipation computed from LES of the isotropic turbulence should be universal for other flows. Therefore, the existence and universality of the optimal CUD will be investigated through LES in the physical space in the following section.

## 5. Simulations in the physical space

In this section, LES of a fully developed channel flow at $Re = 23000$ and of flow past a circular cylinder at $Re = 3900$ are performed in the physical space to investigate the issues addressed in the spectral analysis.

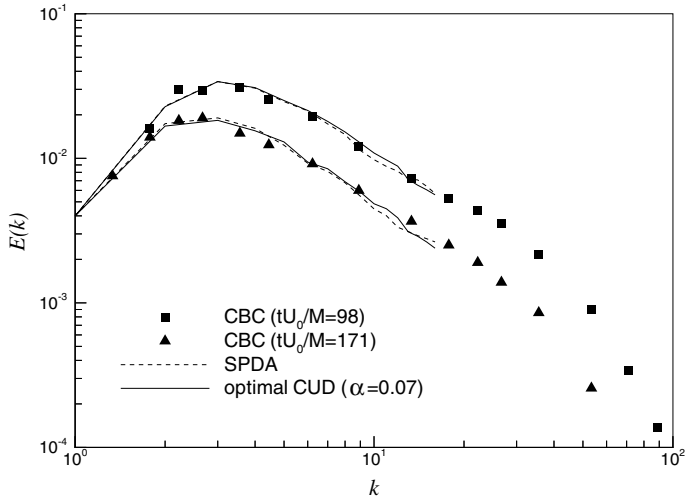


Fig. 13. Time evolution of energy spectra from optimal CUD ($\alpha = 0.07$) compared with those from SPDA.

### 5.1. SGS model and discretization methods

As the governing equation, the compressible formulations of filtered conservation equations for mass, momentum and energy are adopted. For the SGS closure, the compressible variant of DSM [3] is adopted both for momentum and energy equations with Lilly's modification [38]. As a test filter, a top hat filter is used in homogeneous direction(s) with Simpson's 1/3 rule to make the effective ratio of test to grid-filter width be 2.

For the spatial discretization, COM4 and CUD are considered. The conventional temporal discretization schemes for compact differencing such as third-/fourth-order Runge–Kutta schemes introduce a severe temporal stability constraint for wall-bounded viscous flows. To overcome this constraint, we adopt an implicit second-order accurate time integration method [40] based on the scheme due to Ekaterinaris [41], which is an extended version of the Beam–Warming scheme [42] with diagonalization [43] for compact difference schemes. The scheme used here is briefly introduced in Appendix E.

Although the temporal discretization method used in this study is Cauchy stable for linear problems, COM4 is ready to amplify various sources of instability such as the aliasing error, 2-$\Delta$ mode (odd–even decoupling), boundary condition and mesh nonuniformity. To damp out such numerical instabilities, a filtering technique is applied to the conservative variables using an eighth-order compact filter [30,44]:

$$\alpha_f \overline{f}_{i-1} + \overline{f}_i + \alpha_f \overline{f}_{i+1} = \sum_{n=0}^{4} \frac{a_n}{2}(f_{i+n} + f_{i-n}), \tag{32}$$

where $\alpha_f$ is a free parameter in the range of $0 < |\alpha_f| \leqslant 0.5$. The effect of filter decreases as $\alpha_f$ approaches 0.5 and $\alpha_f = 0.5$ leads to no filtering. The coefficients $a_n$ are uniquely determined by the Taylor series expansion [44]: $a_0 = (93 + 70\alpha_f)/128$, $a_1 = (7 + 18\alpha_f)/16$, $a_2 = (-7 + 14\alpha_f)/32$, $a_3 = (1 - 2\alpha_f)/16$ and $a_4 = (-1 + 2\alpha_f)/128$.

To minimize the effect of filter, $\alpha_f$ is set to be as close as 0.5 (a typical value of $\alpha_f$ used in this study is 0.495) and filtering is performed at every 20–40 computational time steps. For all numerical simulations with COM4, we confirmed through an intensive parametric study that filtering does not affect the resolved

scales and only suppresses modes at very high wavenumbers near 2-Δ mode. On the other hand, upwind schemes do not need such filtering due to their dissipative characteristics.

### 5.2. Fully developed channel flow at $Re = 23000$

We consider a fully developed channel flow at $Re = 23000$ based on the centerline velocity $U_c$ and the channel half-width $\delta$. Kravchenko and Moin [9] (KM97) conducted LES of the same flow with various finite difference schemes from CD2 to SPDA by replacing wavenumbers with MWNs in a pseudo-spectral/B-spline code.

For all cases, we adopt the same grid resolution and distribution with those of KM97. A grid of $48 \times 64 \times 48$ is used in the streamwise, wall-normal, and spanwise directions, respectively, in a computational domain of $2\pi\delta \times 2\delta \times \pi\delta/2$, which results in $\Delta x^+ = \Delta x u_\tau/\nu \approx 130$, $\Delta y^+_{\min} \approx 0.5$, $\Delta y^+_{\max} \approx 110$ and $\Delta z^+ \approx 33$. Here $u_\tau$ is the wall shear velocity. Free-stream Mach number $M_\infty = 0.2$ and the Prandtl number $Pr = 0.7$ are chosen in order to make a quasi-incompressible flow condition, and the molecular viscosity is assumed to be constant.

Various simulations are performed with different discretization schemes with and without SGS model. The stability characteristics of these simulations are summarized in Table 1. The computation with COM4 in divergence form are numerically unstable possibly due to the violation of the kinetic energy conservation [9]. This explanation, however, is inappropriate for the present compressible simulation, because the kinetic energy is exchanged with the internal energy and is not conserved. Nevertheless, the conclusions drawn on the incompressible simulation are also valid for the compressible one since there exists an analogue to the kinetic energy conservation: the simulation should satisfy the balance of the turbulent kinetic energy [6] in the limit of no diffusion and without mean flow

$$\int_{\mathscr{V}} \frac{\partial}{\partial t}\left(\frac{1}{2}\rho u_i'' u_i''\right) \mathrm{d}\mathscr{V} + \int_{\mathscr{V}} u_i'' \frac{\partial p}{\partial x_i}\, \mathrm{d}\mathscr{V} = 0, \tag{33}$$

where $\mathscr{V}$ is the computational domain and $u_i'' = u_i - \widetilde{u}_i$ is the fluctuation from the Favre averaging, $\widetilde{u}_i = \overline{\rho u_i}/\bar{\rho}$. The skew-symmetric form satisfies (33) because the summation by part holds numerically even in the presence of the aliasing and finite-differencing errors, but the divergence and advective forms do not satisfy (33) [6,9] (as the product rule of differentiation does not hold for the finite difference schemes). The present simulation with the skew-symmetric form is stable regardless of SGS model, which complies well with the argument given above. The simulation with the advective form is stable only with SGS model, indicating that this form is also affected by the instability due to the violation of (33). Since the conservation property of (33) is independent of discretization errors, in actual simulation, the advantage of the skew-symmetric form comes from both error-minimizing and good conservation characteristics.

Table 1
Simulations of turbulent channel flow with various discretization schemes

| Scheme | Nonlinear terms | SGS model | Stability |
|---|---|---|---|
| COM4 | Divergence | ○ | ↑ |
| COM4 | Skew-symmetric | ○, × | ● |
| COM4 | Advective | ○ (×) | ● (↑) |
| CUDZ | Divergence | ○, × | ↓ |
| CUD3 | Divergence | ○, × | ↓ |
| CUD ($\alpha = 0.008$) | Divergence | ○, × | ● |
| WENO3 | Divergence | ○, × | ↓ |

●, stable; ↑, numerically unstable; ↓, flow laminarizes.

On the other hand, CUDZ, CUD3 and WENO3 laminarize the flow. Among them, the simulation with WENO3 shows the fastest laminarization, which is consistent with the result by Meinke et al. [26] and the dynamic analysis in Appendix C.

The optimal CUD, or CUD with $\alpha = 0.07$ obtained from the isotropic turbulence is tested for this flow. Unfortunately, the scheme is still dissipative and finally laminarizes the flow. Through a parametric study on $\alpha$, we find that there exists a narrow range of $\alpha$ near $\alpha \approx 0.01$ that sustains turbulence, and $\alpha = 0.008$ is the lowest value that does not lead to numerical instability. Therefore, the existence of the optimal upwind scheme that minimizes the total discretization error is again confirmed for this flow, although the amount of optimal dissipation (i.e. values of $\alpha$) is far from being universal.

It is notable from Table 1 that the SGS model does not affect the stability of simulation except for the case of COM4 in the advective form, which is an indirect evidence of the discretization errors being larger than the SGS force for the present flow.

Figs. 14(a) and (b) show the mean streamwise velocity and resolved RMS velocity fluctuations for various schemes listed in Table 1. Also shown are those from SPDA (KM97) and experimental result of Wei and Willmarth [45]. The result from CUDZ is also shown for the purpose of comparison, although it is under laminarization. The mean velocity and RMS velocity fluctuations from COM4-sk with SGS model show an excellent agreement with those from SPDA and the experimental data. The results with COM4-sk without SGS model underestimates the mean velocity and overestimates the RMS velocity fluctuations, which is consistent with KM97 and other LES results without SGS model.

The RMS velocity fluctuations predicted from COM4-adv show a reasonable agreement with those from SPDA, but COM4-adv shows a non-negligible deviation from the log law in the mean velocity profile. The superiority of the skew-symmetric form over the advective form is again confirmed in the physical space simulation.

The result from CUDZ shows excessive numerical dissipation by overpredicting the mean velocity (when plotted in wall unit) and underpredicting the velocity fluctuations. The excessive dissipation seems to be nearly removed by the optimal CUD ($\alpha = 0.008$), predicting a very similar result to that from COM4-adv for both the mean velocity and velocity fluctuations. However, the result from optimal CUD is not as excellent as that from COM4-sk. This trend is analogous to that shown in the dynamic analysis in Section 4.

The spectral aspects of these schemes are demonstrated by the one-dimensional energy spectra in Fig. 15. The spectra from COM4-sk with SGS model agree well with those from SPDA, whereas COM4-sk without

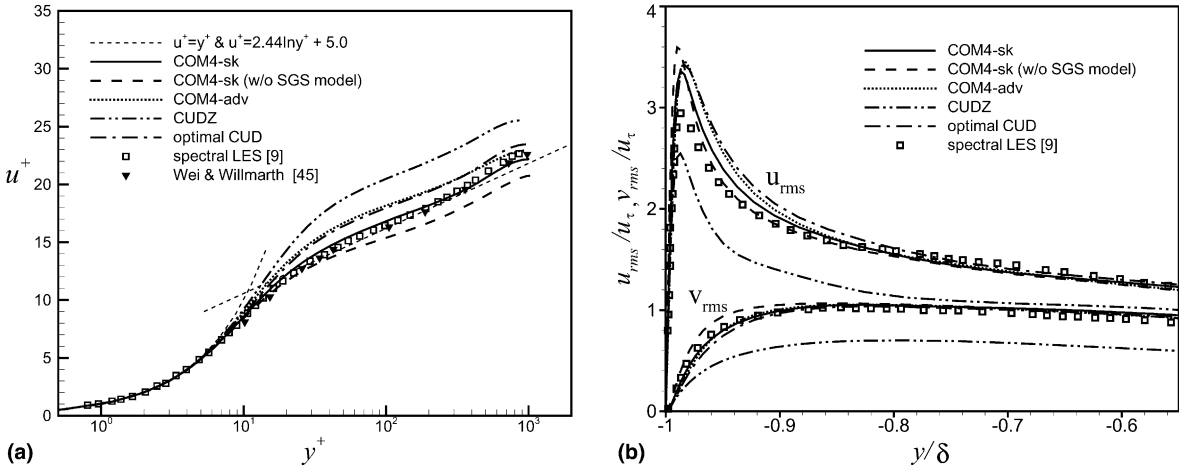


Fig. 14. Statistics for a fully developed channel flow at $Re = 23000$: (a) mean streamwise velocity; (b) RMS velocity fluctuations.

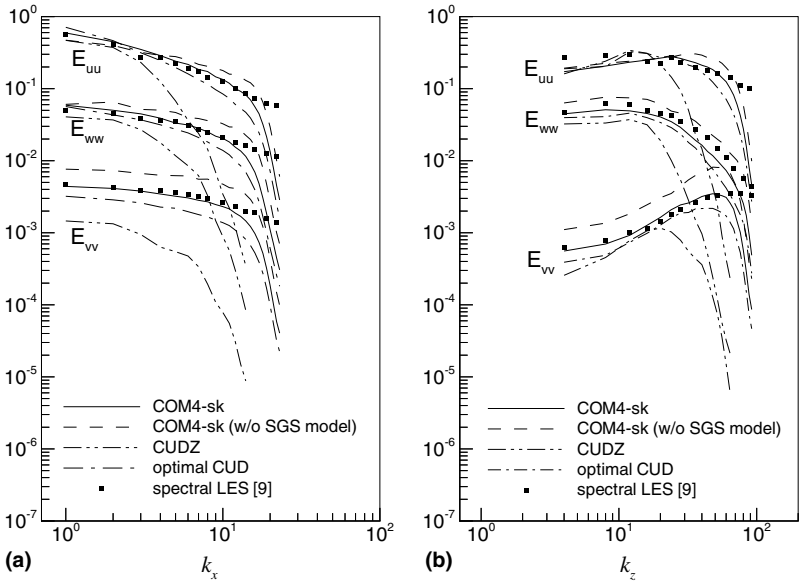


Fig. 15. One-dimensional energy spectra at $y^+ \approx 15$ for a fully developed channel flow: (a) streamwise wavenumber; (b) spanwise wavenumber.

SGS model overpredicts the energy. The optimal CUD slightly underpredicts the energy, but CUDZ significantly damps out the energy at all wavenumbers.

The interaction between the SGS model and the discretization error is estimated by the ratio of the SGS dissipation to total dissipation in Fig. 16, where the results from SPDA and CD2 are taken from KM97. Invoking modified wavenumber argument, the SGS dissipations from COM4-sk and COM4-adv seem to be reasonable. However, due to the numerical dissipation, the SGS dissipation from CUDZ is even smaller that that of CD2 and the qualitative behavior is very different from others. Away from the wall the SGS

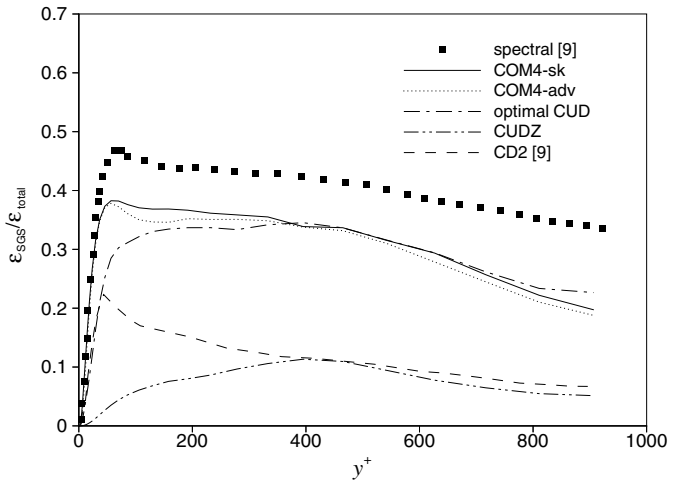


Fig. 16. Ratio of the SGS dissipation to total dissipation for a fully developed channel flow.

dissipation from optimal CUD agrees well with those from COM4-sk and COM4-adv, but is smaller near the wall. Thus, the SGS dissipation is replaced by the numerical dissipation in this region.

Fig. 17 shows the instantaneous vortical structures using the vortex identification method ($\lambda_2$-method) [46]. The elongated structures with spanwise spacings are clearly shown in the case of COM4-sk with SGS model. The estimated steak spacing for this case is roughly 100 in wall units. Without SGS model, the vortical structures become stronger due to no dissipation at unresolved wavenumbers. Fig. 17(c) shows that some streaks are missing in the field from optimal CUD due to the numerical dissipation. However, turbulence seems to survive in this flow when compared with the field from CUDZ where turbulence decays as times goes due to the excessive dissipation.

### 5.3. Flow past a circular cylinder at $Re = 3900$

We consider the flow past a circular cylinder at $Re = 3900$ based on the freestream velocity $U_\infty$ and the diameter $D$. This flow has been one of the most challenging problems for LES that has been tackled with various numerical schemes including CD2 [21,22], QUICK [22], UD7 [19] and B-spline method [47].

Fig. 18 shows the distribution of the grid adopted in this study. An O-type grid with $144 \times 201 \times 48$ points in the azimuthal, radial and spanwise directions is used in a computational domain of $2\pi \times 40D \times \pi D$, respectively. The number of total grid points is nearly same as that used for the Case 2 in [47]. The grid points are clustered near the cylinder surface in the radial direction to retain a nearly uniform grid distribution in $2 < x/D < 12$ and to resolve surface boundary layer. This non-uniform grid distribution is found to be main source of instability for non-dissipative schemes [48]. For COM4, this instability is removed by the eighth-order compact filter with $\alpha_f = 0.495$ (Eq. (32)) per every 20th time step.

Some flow parameters obtained from the computations are summarized in Table 2, together with those from the previous LES [19,21,22,47] and experiments [49–51]. It is interesting to note that the Strouhal number and drag coefficient ($C_D$) can be predicted quite well regardless of the discretization scheme and SGS model used. On the other parameters such as the base-pressure coefficient ($-C_{p_b}$), re-

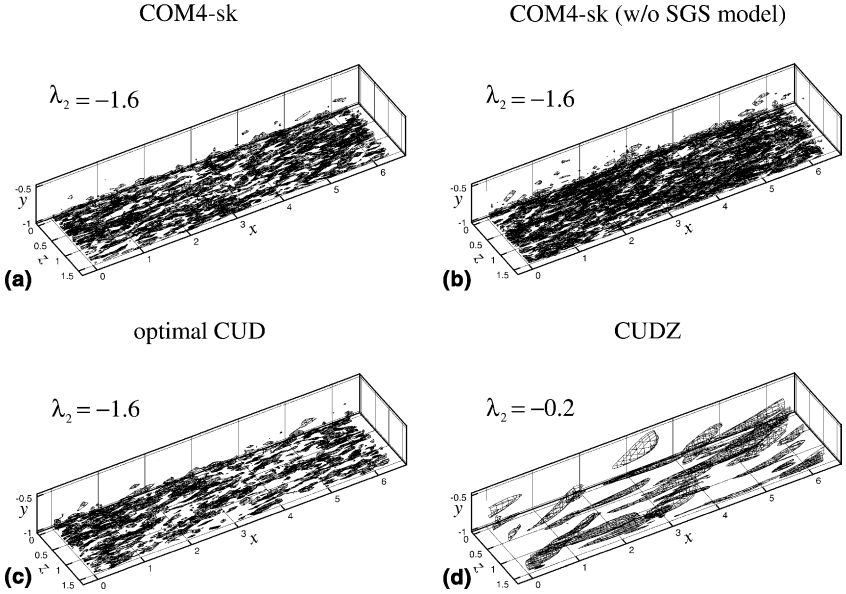


Fig. 17. Instantaneous vortical structures in a fully developed channel flow.

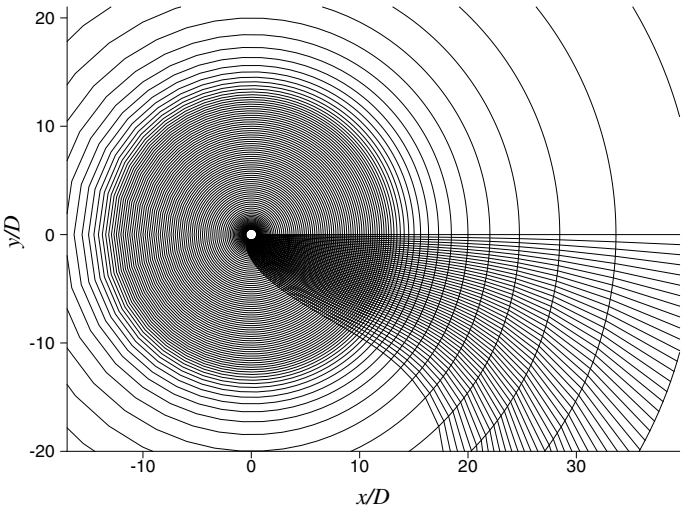


circulation bubble length ($L_{rec}$) and minimum mean streamwise velocity along the centerline ($U_{min}$) seem to be affected by numerical scheme. For example, CUDZ underpredicts $-C_{p_b}$ and $U_{min}$ and overpredicts $L_{rec}$. Similar trends were also observed from the results using UD7 [19] and a QUICK scheme [22] using SM.

In Table 2, we presented the results only from COM4 in the skew-symmetric form and CUDZ. We confirmed that the results from COM4 in the skew-symmetric and divergence forms are nearly identical to each other, indicating that the form of nonlinear term has negligible effects for this flow. This may be due to relatively higher resolution and lower Reynolds number than other flows considered in this paper. Since COM4 in the divergence form predicts the flow very well, the optimal CUD does not exist, i.e. $\alpha = 0$ is the optimal value for this flow. Note that the condition for the existence of an optimal $\alpha$ is that the aliasing and finite-differencing errors should be in comparable magnitude when $\alpha = 0$ as shown in Fig. 12. However, we could not find any sign of the aliasing error such as the pile-up of energy at high wavenumbers from the inspection of the energy spectra at several locations. Therefore, the condition for optimal CUD is not satisfied in the present flow because the finite-differencing error dominates the total discretization error.

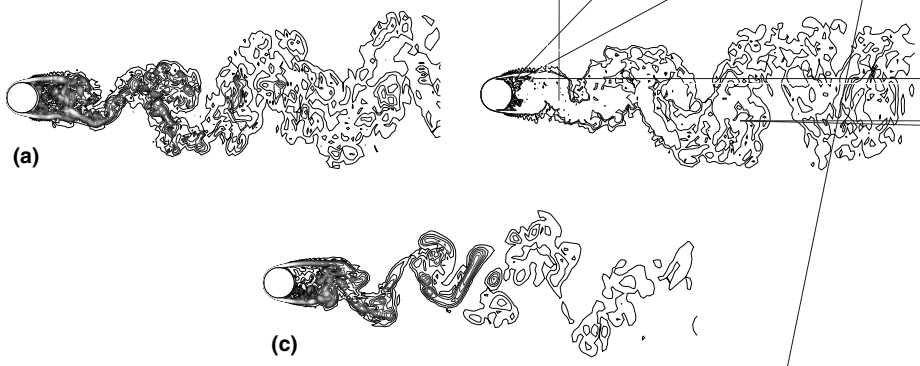


Fig. 19 shows the instantaneous fields showing separating shear layer and Karman vortex street. The vortical structures from COM4-sk without SGS model are stronger than but similar to those with SGS model. Unlike the result from COM4-sk, CUDZ dissipates small-scale structures at $x/D > 3$. Also the length of shear layer from CUDZ is longer than that by COM4-sk, evidently showing the delay of transition from CUDZ, which may be a possible cause of the discrepancies in $-C_{p_b}$, $U_{\min}$ and $L_{\text{rec}}$. Nevertheless, this excessive dissipation by CUDZ is unexpected because the resolution near the cylinder surface is quite sufficient. We found that Van Leer FVS adopted for the present case is responsible for this excessive dissipation in the near-wake region, because the flux does not vanish even for zero velocity due to eigenvalue smoothing. It is a well-known problem of this FVS scheme. Nevertheless, there is no alternative but using Van Leer FVS to avoid an unphysical oscillation near the stagnation point. On the other hand, the dissipation at $x/D > 3$ is purely due to the finite-differencing error.

Figs. 20(a) and (b) show the pressure coefficient and mean streamwise velocity along the centerline of the wake ($y = 0$), respectively. Both the results from COM4-sk with and without SGS model show good agreement with experimental data. Discrepancies observed in the mean streamwise velocity among the numerical and experimental results may result from an earlier transition occurred in the experiment due to

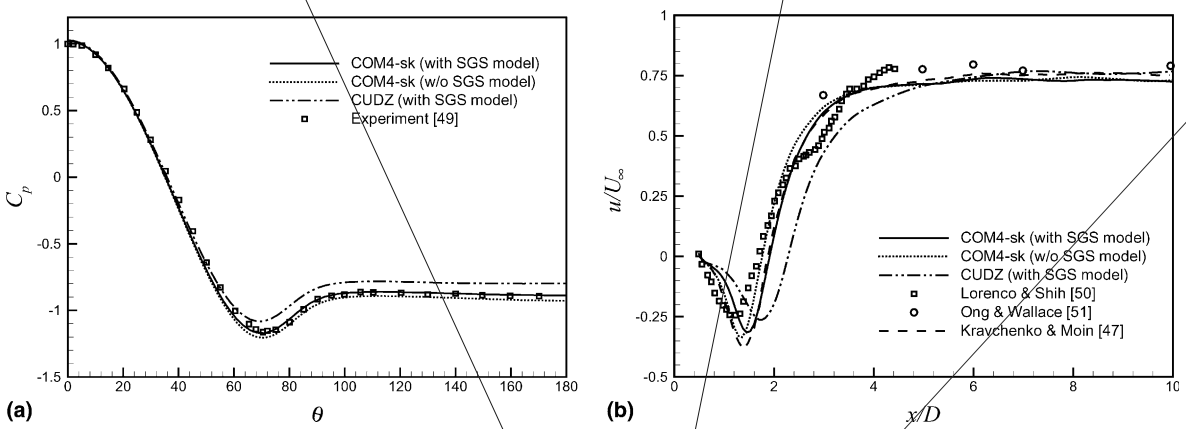


Fig. 20. Statistics for the flow past a circular cylinder at $Re = 3900$: (a) pressure coefficient along the cylinder surface; (b) mean streamwise velocity along the centerline.

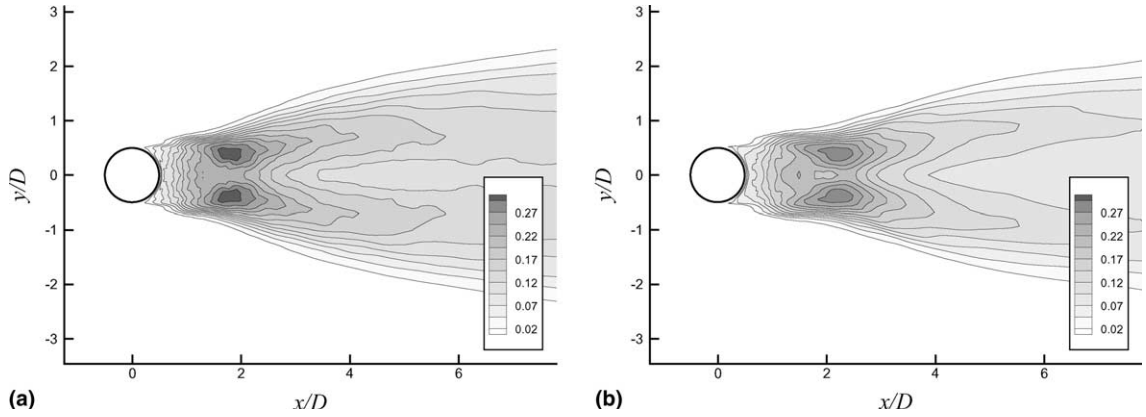


Fig. 21. Ratio of the SGS dissipation to total dissipation. Shown are 12 contours from 0.02 to 0.3: (a) COM4-sk; (b) CUDZ.

background turbulence [47]. Due to the delayed shear layer transition, CUDZ does not predict the base pressure and the mean velocity correctly as shown in Fig. 20(b).

Figs. 21(a) and (b) show the ratio of the SGS dissipation to total dissipation in the near-wake region for COM4-sk and CUDZ, respectively. It is clear that the SGS dissipations from both COM4-sk and CUDZ are small since they do not exceed 30% of total dissipation and are below 15% in the most region. The SGS dissipation from COM4-sk is larger than that from CUDZ, which is consistent with the result from LES of the fully developed channel flow. However, the difference in the results from these two schemes is much smaller for the flow past a circular cylinder.

The one-dimensional frequency spectra at $x/D = 7.0$ and $y/D = 0$ are shown in Fig. 22, together with those from Ong and Wallace [51] and BM94. The spectrum from COM4-sk with SGS model agrees very well with the experimental data [51] and that from Kravchenko and Moin [47] (not shown here) up to the grid cut-off frequency. The spectrum from COM4-sk without SGS model shows also good agreement. However, the spectrum from CUDZ shows a rapid fall-off at high frequencies but is still much better than

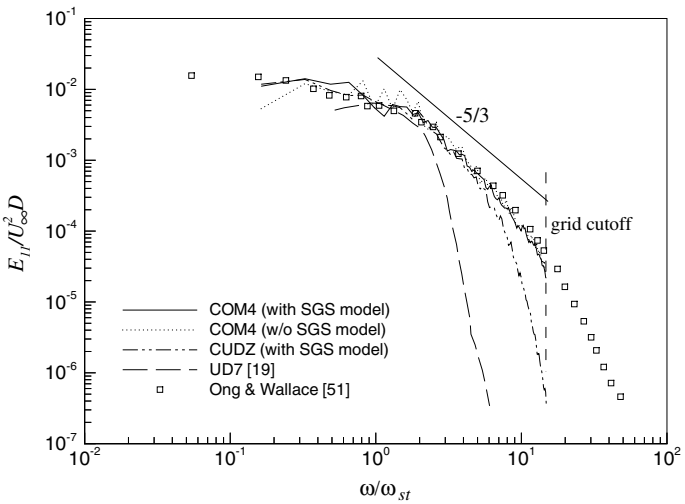


Fig. 22. One-dimensional frequency spectra $E_{11}$ at $x/D = 7$ for the flow past a circular cylinder at $Re = 3900$.

that from UD7 (BM94), although UD7 and CUDZ have nearly the same MWNs as shown in Fig. 1. This result may be explained in terms of the resolution. BW94 used 136 grid points in the radial direction (201 grid points in the present study) and used highly stretched grids along the radial direction, which can be an additional source of numerical dissipation.

## 6. Conclusions

In this paper, the suitability of high-order accurate, centered and upwind-biased compact difference schemes for large eddy simulation was evaluated by the static and dynamic analyses. The static error analysis indicated that both the finite-differencing and aliasing errors increase as the amount of numerical dissipation increases. On the other hand, the dynamic error analysis led to nearly opposite conclusions in that the aliasing error decreases as the numerical dissipation increases and the finite-differencing error overweighs the aliasing error. From the comparison of both analyses, we concluded that the discretization errors are properly characterized only by the dynamic analysis.

For the decaying isotropic turbulence, we showed the existence of optimal amount of dissipation that minimizes total discretization error, when compact upwind schemes were used. However, the amount of optimal dissipation was very small, clearly explaining the failure of conventional upwind schemes in LES. It was also shown that upwind schemes considered in this study satisfy none of the conditions C1 and C2 explained in Section 1; i.e. the dissipative finite-differencing error of upwind schemes is larger than the SGS dissipation, and the spectral behavior of the finite-differencing error is not similar to that of the SGS dissipation. In addition, a classical issue on the formulation of nonlinear term was revisited to show that the skew-symmetric form minimizes both the finite-differencing and aliasing errors among all the possible forms.

Finally, LES of turbulent channel flow at $Re = 23000$ and flow over a circular cylinder at $Re = 3900$ were performed. The results showed that conventional compact upwind schemes are not suitable for LES, whereas the fourth-order compact centered scheme is a good candidate for LES provided that a proper treatment of nonlinear term is performed. The existence of optimal upwind scheme was also verified in the physical space simulation, although the amount of optimal dissipation was significantly dependent on the flow type.

## Acknowledgements

This work is supported by the BK 21 Program through the Korean Ministry of Education and Human Resources Development, and by the Creative Research Initiatives through the Korean Ministry of Science and Technology.

## Appendix A. Subgrid-scale modelling errors

In this appendix, we estimate the SGS modeling error as compared to the true SGS force. For this purpose, three different SGS models are considered here.

- Spectral eddy viscosity model (SPEVM) [37].

  In the Fourier space, SPEVM assumes the SGS force as

$$F_i^{>}(\mathbf{k}) = \mathscr{P}(\mathrm{i}k_j\hat{\tau}_{ij}(\mathbf{k})) = -\nu^t(k|k_c)k^2\hat{u}_i(\mathbf{k}), \tag{A.1}$$

where $k_c$ is the cut-off wavenumber, and the spectral eddy viscosity $\nu^t$ is given by

$$v^t(k|k_c) = v^{t+}(k|k_c)\left(\frac{E(k_c,t)}{k_c}\right)^{1/2}, \tag{A.2}$$

$$v^{t+}(k|k_c) = 0.267\left(1 + 34.5e^{-3.03(k_c/k)}\right). \tag{A.3}$$

- Fixed-coefficient Smagorinsky model (SM) and dynamic Smagorinsky model (DSM) [2,38].
  The Smagorinsky model assumes the SGS stress as

$$\tau_{ij} - \frac{1}{3}\tau_{kk}\delta_{ij} = -2C_s\Delta^2|\overline{S}|\,\overline{S_{ij}}, \tag{A.4}$$

where $|\overline{S}| = \sqrt{2\overline{S}_{ij}\overline{S}_{ij}}$, and $\tau_{kk}$ is not modeled in incompressible flow but absorbed in the pressure term. The Smagorinsky constant $C_s$ is a global constant in space and time for SM. In DSM [2,38], it is determined by

$$C_s\Delta^2 = -\frac{1}{2}\frac{\langle L_{ij}M_{ij}\rangle}{\langle M_{ij}M_{ij}\rangle}, \tag{A.5}$$

where $\langle\ \rangle$ denotes the average over homogeneous direction(s), and

$$L_{ij} = \widetilde{\overline{u_i}\,\overline{u_j}} - \widetilde{\overline{u_i}}\,\widetilde{\overline{u_j}}, \tag{A.6}$$

$$M_{ij} = \left(\frac{\tilde{\Delta}}{\Delta}\right)^2 |\widetilde{\overline{S}}|\,\widetilde{\overline{S_{ij}}} - \widetilde{|\overline{S}|\,\overline{S_{ij}}}. \tag{A.7}$$

The tilde denotes the test filtering with a filter width $\tilde{\Delta}$ wider than that of grid filter $\Delta$. Usually $\tilde{\Delta}/\Delta = 2$ is taken.

Fig. 23 shows PSDs of SGS forces computed from SPEVM, SM and DSM, toghether with PSD of discrete true SGS force described in Section 3.1.3. For SM, $C_s = 0.01$ is used, and $C_s$ is dynamically determined to be about 0.0072 in DSM.

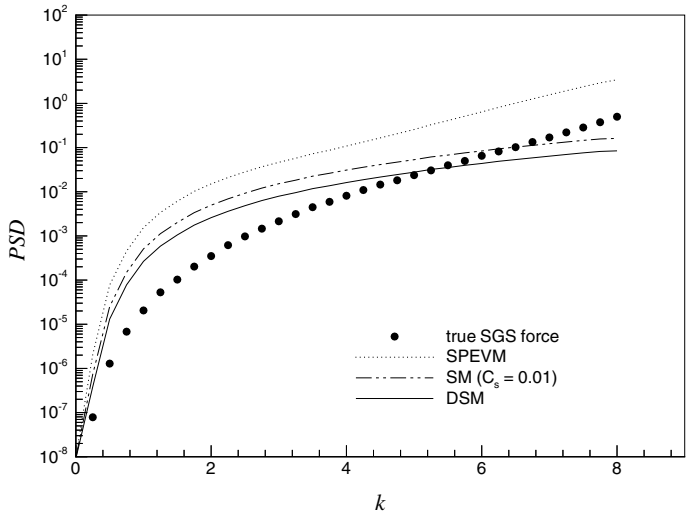


Fig. 23. Power spectra of SGS forces from typical models as compared with true SGS force.

PSD from SPEVM overestimates the SGS force at all wavenumbers, which means that excessive SGS dissipation would be supplied by the model. PSDs from SM and DSM show better agreements with true SGS force, but overestimate the SGS force at low wavenumbers and underestimate it at high wavenumbers. This is not surprising because previous a priori tests [34,52] reported that the correlation between $\tau_{ij}$ and $|\overline{S}|\overline{S}_{ij}$ is very low.

PSDs of modeled SGS forces provide a new insight regarding the effect of models on the energy transfer between various scales of turbulent motion. For example, when SM is used, one may explain an excessive dissipation in mid-wavenumbers and pile-up near cut-off wavenumber observed in LES of isotropic turbulence (see, e.g. [53]).

In spite of such a non-negligible SGS modelling error, we do not seriously consider it in this paper because only the discretization error matters as far as an LES result from a modeled SGS force and exact discretization schemes is regarded as an exact solution. In this respect, the SGS modelling error would play only a passive role in determining discretization errors. Moreover, the velocity-stress (or SGS dissipation) correlation for the eddy viscosity model is remarkably high [52,54], so that the model complies reasonably well with the necessary conditions [54] to accurately reproduce the energy spectrum of the resolved velocity in grid turbulence.

## Appendix B. One-dimensional analysis on the aliasing error

To further investigate the effect of upwinding on the aliasing error, one-dimensional analysis is performed with a simple nonlinear term as considered in [9]. Let us define scalar functions $u(x)$ and $v(x)$ on $0 \leqslant x \leqslant 2\pi$ and consider the numerical approximations of $N \equiv \mathrm{d}uv/\mathrm{d}x$. $u$ and $v$ are assumed to be positive and have the Fourier coefficients $\hat{u}(k) = \hat{v}(k) = \sqrt{E(k)}$, where $E(k)$ is the Von Karman spectrum defined by (27) with $k_p = 1$. If $u_i$ and $v_i$ are the projections of $u$ and $v$ onto discrete and uniform grid points $x_i$ $(i = 0, 1, \ldots, M)$, possible candidates for the discrete evaluation of $N$ are

$$\begin{aligned} N_1 &= \frac{\delta uv}{\delta x}, \\ N_2 &= u\frac{\delta v}{\delta x} + v\frac{\delta u}{\delta x}, \\ N_3 &= \frac{1}{2}(N_1 + N_2). \end{aligned} \tag{B.1}$$

Here, $N_1$, $N_2$, and $N_3$ correspond to one-dimensional analogues of the divergence, advective and skew-symmetric forms, respectively, as defined in (3). By Fourier transforming these terms, we get

$$\begin{aligned} \hat{N}_1(k) &= \mathrm{i}k'(k)\left(\sum_{n+m=k}\hat{u}(n)\hat{v}(m) + \sum_{n+m=k\pm M}\hat{u}(n)\hat{v}(m)\right), \\ \hat{N}_2(k) &= \sum_{n+m=k}\Big(\hat{u}(n)\mathrm{i}k'(m)\hat{v}(m) + \mathrm{i}k'(n)\hat{u}(n)\hat{v}(m)\Big) \\ &\quad + \sum_{n+m=k\pm M}\Big(\hat{u}(n)\mathrm{i}k'(m)\hat{v}(m) + \mathrm{i}k'(n)\hat{u}(n)\hat{v}(m)\Big), \\ \hat{N}_3(k) &= \frac{1}{2}\Big(\hat{N}_1 + \hat{N}_2\Big), \end{aligned} \tag{B.2}$$

where the second terms in $\hat{N}_1$ and $\hat{N}_2$ are the aliasing errors. If we denote these terms as $E_i^{\mathrm{alias}}(k)$, PSD of the aliasing errors can be defined as $\mathscr{E}_i^{\mathrm{alias}}(k) = (2\pi/L)E_i^{\mathrm{alias}}(k) \cdot E_i^{\mathrm{alias}*}(k)$. As MWN of upwind scheme can be represented as $k' = k_r + \mathrm{i}k_i$ $(k_r, k_i \in R)$, PSD of the aliasing error for the divergence form is

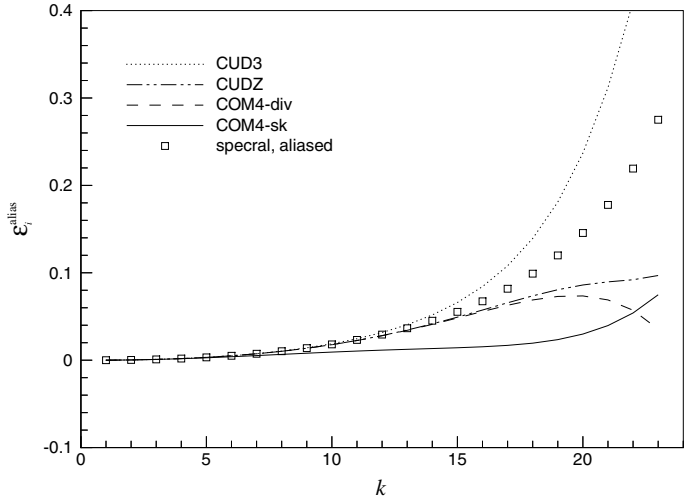


Fig. 24. Aliasing errors for various schemes with one-dimensional Von Karman spectrum.

$$\mathscr{E}_1^{\text{alias}}(k) = \left(k_r^2 + k_i^2\right)\left(\sum_{n+m=k\pm M} \sqrt{E(n)E(m)}\right)^2. \tag{B.3}$$

From (B.3), it is manifest that the imaginary part of MWN increases PSD of the aliasing error. For example, the aliasing error from UD5 is larger than that of CD6 at all wavenumbers because two schemes have the same real part of MWN. The same conclusion holds for other pairs of upwind and central schemes such as UD1 and CD2, or UD7 and CD8.

Fig. 24 shows PSDs of the aliasing errors of CUD3, CUDZ, COM4-div, COM4-sk and aliased spectral method in the divergence form with $M = 48$. As the consequence of the definition given by (B.3), the aliasing error of CUD3 is even larger than that of the aliased spectral method. Again, except near the cut-off wavenumber, the skew-symmetric form leads to the lowest aliasing error because the aliasing errors of $\hat{N}_1$ and $\hat{N}_2$ have opposite signs [7,9].

## Appendix C. Additional sources of numerical dissipation

The characteristic of a central difference scheme is completely described with its modified wavenumber. However, it is not the case for nonlinear upwind schemes whose MWN cannot be defined, and even for linear upwind scheme due to flux vector splitting. In this appendix, the effect of FVS and shock-capturing scheme on the numerical dissipation is investigated.

First, we consider a popular flux splitting scheme, global Lax–Friedrichs splitting (GLF-FVS) [13] defined as

$$f^{\pm}(u) = \frac{1}{2}(f(u) \pm |c|u), \tag{C.1}$$

where $c$ is usually taken as the largest eigenvalue of the function $f(u)$ over the entire domain. Let us introduce MWNs for the first and second derivatives, $k' = k_r + \mathrm{i}k_i$ and $k''$, and consider the Burgers equation with $f(u) = (1/2)u^2$ in the Fourier space

$$\left(\frac{\partial}{\partial t}+\nu k''\right)\hat{u}_k=-\frac{1}{2}\mathrm{i}k'\left(\hat{f}_k+|c|\hat{u}_k\right)-\frac{1}{2}\mathrm{i}k'^{*}\left(\hat{f}_k-|c|\hat{u}_k\right). \tag{C.2}$$

Substituting $k'=k_r+\mathrm{i}k_i$ into (C.2) leads to

$$\left(\frac{\partial}{\partial t}+\nu k''-|c|k_i\right)\hat{u}_k=-\mathrm{i}k_r\hat{f}_k=-\frac{\mathrm{i}}{2}k_r\left(\sum_{p+q=k}\hat{u}(p)\hat{u}(q)+\sum_{p+q=k\pm M}\hat{u}(p)\hat{u}(q)\right), \tag{C.3}$$

where $M$ is the number of grid points. As is clear in (C.3), an additional linear finite-differencing error, $-|c|k_i\hat{u}_k$, is introduced due to GLF-FVS. Note that $k_i\leqslant 0$ for all wavenumbers and $|c|\sim \mathrm{O}(1)$ for a properly nondimensionalized system. Therefore, $-|c|k_i\gg \nu k''$ except for very low Reynolds number flows. This implies that the accuracy of high-order upwind schemes can be considerably masked by the false diffusion due to FVS.

The failure of GLF-FVS comes from the fact that the splitted nonlinear flux produces an additional linear term which causes the monotonic decay of $\hat{u}_k$ in time with the decay rate of $-|c|k_i$. On the other hand, other flux splitting schemes such as LLF, Steger–Warming [55] and Van Leer splitting [31] do not have such a problem as they let nonlinear terms be nonlinear after splitting. However, Steger–Warming and Van Leer FVS suffer from oscillations near stagnation/sonic points or excessive dissipation in the boundary layer as addressed in Section 5.3. Roe's flux-difference splitting [56] and AUSM [29] are widely used as alternatives, but they are not considered in the present study because CUD cannot be implemented with them as they require flux reconstruction (interpolation) schemes.

To see the effect of FVS on the solution of the Navier–Stokes equation, we revisit both the static and dynamic error analyses. Fig. 25(a) shows PSDs of the finite-differencing error for LLF-FVS and GLF-FVS. The finite-differencing error from GLF-FVS is an order of magnitude larger at all wavenumbers than that from LLF-FVS. Fig. 25(b) shows the results from simulation of CBC-isotropic turbulence using both splitting schemes. CUDZ with GLF-FVS shows a highly dissipative nature at high wavenumbers and produces excessive energy at intermediate wavenumbers. A similar trend was observed from the QUICK scheme [57]. From the present results, it is clear that the way of splitting the nonlinear flux is as important as the difference scheme itself, and the use of linear splitting schemes such as GLF-FVS should be avoided in LES.

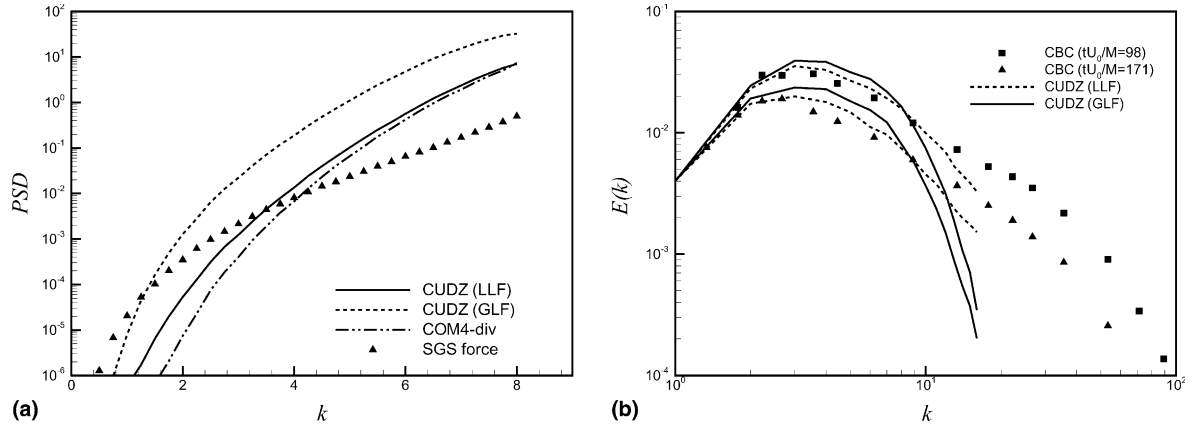


Fig. 25. Effect of flux vector splitting schemes on the finite-differencing error: (a) power spectral density of the finite-differencing error; (b) energy spectra for decaying turbulence.

Next, the effect of shock-capturing scheme is investigated. We consider a class of strongly conservative, flux reconstruction scheme

$$\frac{\delta f(u)}{\delta x} = \frac{1}{h}\left(\widetilde{f}_{i+1/2} - \widetilde{f}_{i-1/2}\right), \tag{C.4}$$

where $\widetilde{f}_{i\pm1/2}$ denotes the numerical flux at the staggered node (or the cell face), which can be decomposed as $\widetilde{f}_{i+1/2} = \widetilde{f}^{+}_{i+1/2} + \widetilde{f}^{-}_{i+1/2}$. Therefore, the reconstruction of numerical fluxes is the core procedure for difference schemes of this type. TVD-MUSCL [58] , ENO [59] and WENO [12,13] are popular reconstruction schemes. Among them, we consider WENO3 [13]. WENO3 computes the numerical flux defined in (C.4) as

$$\begin{aligned}
\widetilde{f}^{+}_{i+1/2} &= \omega^{+}_{0}\left(\frac{1}{3}f^{+}_{i-2} - \frac{7}{6}f^{+}_{i-1} + \frac{11}{6}f^{+}_{i}\right) + \omega^{+}_{1}\left(-\frac{1}{6}f^{+}_{i-1} + \frac{5}{6}f^{+}_{i} + \frac{1}{3}f^{+}_{i+1}\right) \\
&\quad + \omega^{+}_{2}\left(\frac{1}{3}f^{+}_{i} + \frac{5}{6}f^{+}_{i+1} - \frac{1}{6}f^{+}_{i+2}\right), \\
\omega^{+}_{k} &= \frac{\alpha^{+}_{k}}{\sum_{k=0}^{2}\alpha^{+}_{k}}, \quad k = 0,1,2, \\
\alpha^{+}_{k} &= C_{k}\left(\epsilon + IS^{+}_{k}\right)^{-2},
\end{aligned} \tag{C.5}$$

where $\epsilon = 10^{-6}$ and $C_k$ are optimal weights given by $C_0 = 1/10$, $C_1 = 6/10$ and $C_2 = 3/10$. $IS_k$ are smoothness indicators that can be constructed in a number of ways. We adopt the following formulation [13]:

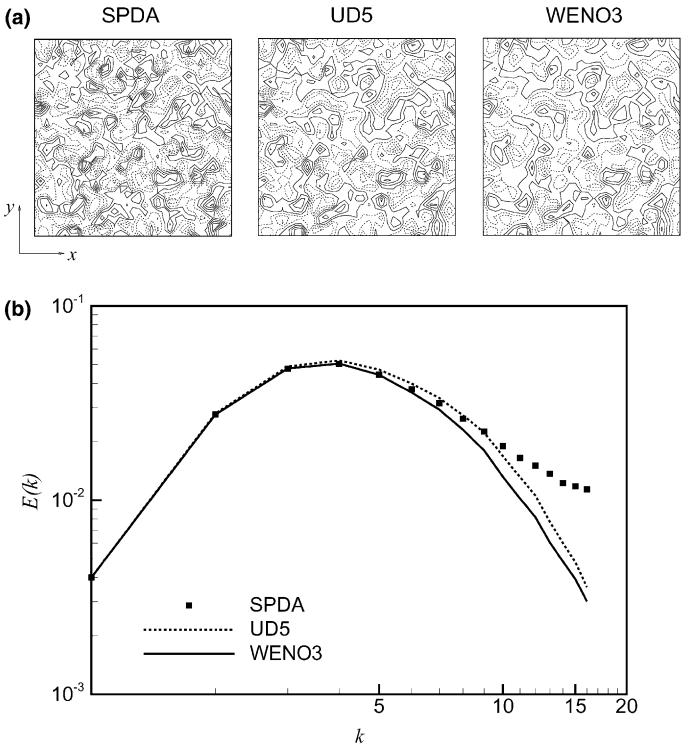


Fig. 26. Effect of shock-capturing scheme on the numerical dissipation: (a) instantaneous $\omega_z$ contours on an $x$–$y$ plane at $tU_0/M = 64$; (b) energy spectra at $tU_0/M = 64$.

$$
\begin{aligned}
IS_0^+ &= \frac{13}{12}\left(f_{i-2}^+ - 2f_{i-1}^+ + f_i^+\right)^2 + \frac{1}{4}\left(f_{i-2}^+ - 4f_{i-1}^+ + 3f_i^+\right)^2,\\
IS_1^+ &= \frac{13}{12}\left(f_{i-1}^+ - 2f_i^+ + f_{i+1}^+\right)^2 + \frac{1}{4}\left(f_{i-1}^+ - f_{i+1}^+\right)^2,\\
IS_2^+ &= \frac{13}{12}\left(f_i^+ - 2f_{i+1}^+ + f_{i+2}^+\right)^2 + \frac{1}{4}\left(3f_i^+ - 4f_{i+1}^+ + f_{i+2}^+\right)^2.
\end{aligned}
\tag{C.6}
$$

Similarly, the numerical flux for negative part is given by the symmetric formulation to (C.5) and (C.6). WENO3, like other flux reconstruction schemes, is nonlinear due to smoothness indicators. Thus, MWN cannot be defined for such a scheme. However, for smooth flows where $IS_k$ approach zero, it is easy to show that WENO3 reduces to UD5. However, it is questionable whether WENO3 treats marginally resolved turbulent flows as 'smooth' fields or not. For these flows, steep gradients of the flow variables inevitably arise due to nonlinear interactions, which result in the increase in the smoothness indicator, $IS_k$ in (C.6). Once high $IS_k$ is detected in one candidate stencil, WENO3 underestimates the contribution from this stencil by scoring a lower weight to that than to other stencils. Therefore, such a nonlinear shock-capturing scheme can be an additional source of numerical dissipation.

In order to verify this scenario, WENO3 is tested for CBC-isotropic turbulence. Because MWN cannot be defined, the derivative is obtained in the physical space. Fig. 26(a) shows the instantaneous vorticity ($\omega_z$) contours from SPDA, UD5 and WENO3 on an $x$–$y$ plane at $tU_0/M = 64$. The energy spectra at the same time are plotted in Fig. 26(b). It is clear that a further dissipation is generated by WENO3 to the flow field obtained from UD5. Therefore, shock-capturing schemes are not good candidates for LES since they rapidly dissipate small scales.

## Appendix D. Miles approach

In MILES, the dissipation error by upwind schemes is considered as a built-in SGS model and no explicit SGS model is used. Furthermore, the viscous term in the Navier–Stokes equation is often neglected. In the present MILES, we also neglect the viscous term.

Fig. 27 shows the energy spectra at $tU_0/M = 98$ and the decay of the resolved kinetic energy for LES and MILES with CUD3 and WENO3. For CUD3, both LLF-FVS and GLF-FVS are considered. MILES

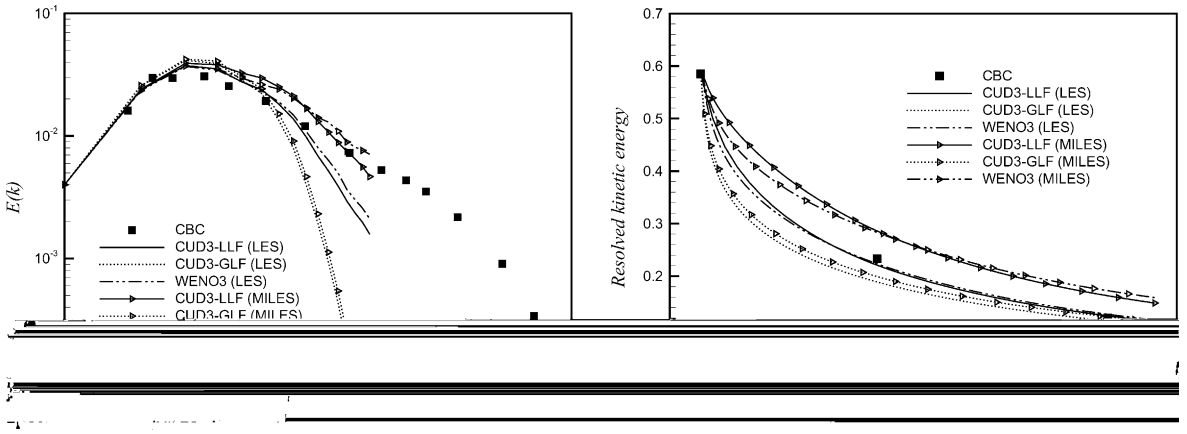


Fig. 27. Results from LES and MILES with CUD3 and WENO3: (a) energy spectra at $tU_0/M = 98$; (b) decay of the resolved kinetic energy.

provides stable solutions and roughly reproduces the decay of resolved kinetic energy. This result supports the concept of MILES. However, among all the results shown in Fig. 27, the best agreement with the CBC result is obtained from LES with CUD3-LLF and WENO3. The results from MILES with CUD3-LLF and WENO3 indicate that an additional dissipation at intermediate wavenumbers is required to suppress excessive energy at these scales. Therefore, the condition C2 (numerical dissipation should be able to produce the appropriate amount of SGS dissipation) is not satisfied by the present upwind schemes. The present result is consistent with the conclusion of Garnier et al. [23], who performed MILES with shock-capturing schemes such as ENO, TVD and Jameson schemes. On the other hand, the results from both LES and MILES with CUD3-GLF are contaminated by the finite-differencing error due to GLF-FVS.

## Appendix E. Implementation of compact difference schemes in the implicit time marching schemes

In this appendix, we present an implicit temporal discretization scheme combined with compact difference schemes, which is used in the physical space simulations in Section 5. For simplicity, we consider the following two-dimensional Euler equation in the curvilinear coordinates $(\xi,\eta)$:

$$\frac{\partial \mathbf{Q}}{\partial t}+\frac{\partial \mathbf{E}(\mathbf{Q})}{\partial \xi}+\frac{\partial \mathbf{F}(\mathbf{Q})}{\partial \eta}=0, \tag{E.1}$$

where $\mathbf{Q}=J^{-1}[\rho,\rho u,\rho v,e]^{\mathrm{T}}$ is the solution vector, $J$ is the Jacobian of the coordinate transformation, and $\mathbf{E}$ and $\mathbf{F}$ are flux vectors in curvilinear coordinates. For example, $\mathbf{E}=J^{-1}(\xi_x\mathbf{e}+\xi_y\mathbf{f})=\mathbf{J}^{-1}[\rho U,\rho uU+\xi_x p,\rho vU+\xi_y p,(E_T+p)U-\xi_t p]^{\mathrm{T}}$, where $\mathbf{e}$ and $\mathbf{f}$ are flux vectors in the Cartesian coordinates $(x,y)$ and $U$ is the contravariant velocity component $U=\xi_x u+\xi_y v+\xi_t$.

When we apply the Crank–Nicolson scheme to (E.1) for the physical time marching, a linearized semi-discretized system is given by

$$\Delta\mathbf{Q}^p_{i,j}+\frac{\Delta t}{2}\partial_\xi(\mathbf{A}\Delta\mathbf{Q})^p_{i,j}+\frac{\Delta t}{2}\partial_\eta(\mathbf{B}\Delta\mathbf{Q})^p_{i,j}=R^p_{i,j}, \tag{E.2}$$

where $\Delta\mathbf{Q}^p=\mathbf{Q}^{p+1}-\mathbf{Q}^p$, $R^p_{i,j}=\mathbf{b}_{i,j}-\Delta t(\partial_\xi\overline{\mathbf{E}}_{i,j}+\partial_\eta\overline{\mathbf{F}}_{i,j})$, $\mathbf{b}_{i,j}=\mathbf{Q}^n_{i,j}-\mathbf{Q}^p_{i,j}$, $\overline{\mathbf{E}}=(1/2)(\mathbf{E}^p+\mathbf{E}^n)$, and $\overline{\mathbf{F}}=(1/2)(\mathbf{F}^p+\mathbf{F}^n)$. The superscript $^p$ refers to the number of nonlinear subiterations used during time advancement from time level $n$ to the new level $n+1$ with the physical time step $\Delta t$ in order to eliminate the linearization error, and $\mathbf{A}=\partial\mathbf{E}/\partial\mathbf{Q}$ and $\mathbf{B}=\partial\mathbf{F}/\partial\mathbf{Q}$ are the Jacobian matrices.

The spatial accuracy of the scheme is determined by that of the differencing scheme adopted for the terms in RHS of (E.2). This justifies the use of low-order schemes such as UD1 or CD2 for the implicit part of such linearized systems to reduce the bandwidth of the global matrix (see, e.g. [20,44]). However, our numerical experience indicates that such a method poses a severe stability problem when the explicit terms are discretized with non-dissipative high-order schemes, which often leads to solution blow-up.

As an alternative, Ekaterinaris [41] proposed a new temporal implementation scheme that uses COM4 for both LHS and RHS of (E.2). We use a similar method to that in [41]. First, let us introduce a weighted summation over adjacent grid points, which is defined for any $\phi$ as

$$\phi_{[4]i}=\phi_{i-1}+4\phi_i+\phi_{i+1}. \tag{E.3}$$

With the approximate factorization and the weighted summation to (E.2) both in $\xi$- and $\eta$-directions, we get

$$\left[\mathbf{I}+\frac{\Delta t}{2}\partial_\xi\mathbf{A}\right]\left[\mathbf{I}+\frac{\Delta t}{2}\partial_\eta\mathbf{B}\right]\Delta\mathbf{Q}^p_{[4]i,[4]j}=R^p_{[4]i,[4]j}. \tag{E.4}$$

Solution of (E.4) is replaced by the sequential solutions of two equations

$$\left[\mathbf{I}+\frac{\Delta t}{2}\partial_\xi \mathbf{A}\right]\mathbf{S}_{[4]i,j}=R^p_{[4]i,[4]j}, \tag{E.5}$$

$$\left[\mathbf{I}+\frac{\Delta t}{2}\partial_\eta \mathbf{B}\right]\Delta\mathbf{Q}^p_{i,[4]j}=\mathbf{S}_{i,j}. \tag{E.6}$$

Applying COM4 to the derivatives in LHS of (E.5) and (E.6), they become

$$\left(\mathbf{I}-\frac{3\Delta t}{2\Delta\xi}\mathbf{A}\right)\mathbf{S}_{i-1,j}+4\mathbf{S}_{i,j}+\left(\mathbf{I}+\frac{3\Delta t}{2\Delta\xi}\mathbf{A}\right)\mathbf{S}_{i+1,j}=R^p_{[4]i,[4]j}, \tag{E.7}$$

$$\left(\mathbf{I}-\frac{3\Delta t}{2\Delta\eta}\mathbf{B}\right)\Delta\mathbf{Q}^p_{i,j-1}+4\Delta\mathbf{Q}^p_{i,j}+\left(\mathbf{I}+\frac{3\Delta t}{2\Delta\eta}\mathbf{B}\right)\Delta\mathbf{Q}^p_{i,j+1}=\mathbf{S}_{i,j}, \tag{E.8}$$

where a fourth-order Padé approximation, e.g.,

$$\partial_\xi(\mathbf{AS})_{i-1}+4\partial_\xi(\mathbf{AS})_i+\partial_\xi(\mathbf{AS})_{i+1}\approx\frac{3}{\Delta\xi}\left\{(\mathbf{AS})_{i+1}-(\mathbf{AS})_{i-1}\right\} \tag{E.9}$$

is used in (E.7) and (E.8). Applying COM4 to RHS, $R^p_{[4]i,[4]j}$ is simplified

$$\begin{aligned}R^p_{[4]i,[4]j}&=\mathbf{b}_{[4]i,[4]j}-\Delta t\left(\partial_\xi\overline{\mathbf{E}}_{[4]i,[4]j}+\partial_\eta\overline{\mathbf{F}}_{[4]i,[4]j}\right)\\&=\mathbf{b}_{i-1,j-1}+4\mathbf{b}_{i,j-1}+\mathbf{b}_{i+1,j-1}+4\left(\mathbf{b}_{i-1,j}+4\mathbf{b}_{i,j}+\mathbf{b}_{i+1,j}\right)+\mathbf{b}_{i-1,j+1}+4\mathbf{b}_{i,j+1}+\mathbf{b}_{i+1,j+1}\\&\quad-\frac{3\Delta t}{\Delta\xi}\left(\overline{\mathbf{E}}_{i+1}-\overline{\mathbf{E}}_{i-1}\right)_{[4]j}-\frac{3\Delta t}{\Delta\eta}\left(\overline{\mathbf{F}}_{j+1}-\overline{\mathbf{F}}_{j-1}\right)_{[4]i},\end{aligned} \tag{E.10}$$

where a Padé approximation as in (E.9) is also applied to $\partial_\xi\overline{\mathbf{E}}_{[4]i}$ and $\partial_\eta\overline{\mathbf{F}}_{[4]j}$. Therefore, with the weighted summation (E.3) and Padé approximation, we obtain a fully discretized system (E.7), (E.8) and (E.10). Two block-tridiagonal matrices, (E.7) and (E.8), are directly inverted by the Thomas algorithm.

The present scheme differs from that of Ekaterinaris [41] in that the weighted summations are applied to both directions simultaneously, which enables us to use (E.10). By using (E.10), the computational cost is saved up to 30% as no matrix inversion is required to get derivatives of the flux vectors with COM4.

## References

[1] P. Moin, Advances in large eddy simulation methodology for complex flows, Int. J. Heat Fluid Flow 23 (2002) 710.
[2] M. Germano, U. Piomelli, P. Moin, W. Cabot, A dynamic subgrid-scale eddy viscosity model, Phys. Fluids A 3 (1991) 1760.
[3] P. Moin, K. Squires, W. Cabot, S. Lee, A dynamic subgrid scale model for compressible turbulence and scalar transport, Phys. Fluids A 3 (1991) 2746.
[4] J.A. Domaradzki, K.C. Loh, The subgrid-scale estimation model in the physical space representation, Phys. Fluids 11 (1999) 2330.
[5] T.A. Zang, On the rotation and skew-symmetric forms for incompressible flow simulations, Appl. Numer. Math. 7 (1991) 27.
[6] G.A. Blaisdell, N.N. Mansour, W.C. Reynolds, Numerical simulation of compressible homogeneous turbulence, Report No. TF-50, Department of Mechanical Engineering, Stanford University, 1991.
[7] I. Fedoiun, N. Lardjane, I. Gokalp, Revisiting numerical errors in direct and large eddy simulations of turbulence: physical and spectral space analysis, J. Comput. Phys. 174 (2001) 816.
[8] S. Ghosal, An analysis of numerical errors in large-eddy simulations of turbulence, J. Comput. Phys. 125 (1996) 187.
[9] G. Kravchenko, P. Moin, On the effect of numerical errors in large-eddy simulations of turbulent flows, J. Comput. Phys. 131 (1997) 310.

[10] F.K. Chow, P. Moin, A further study of numerical errors in large-eddy simulations, J. Comput. Phys. 184 (2003) 366.
[11] B. Vreman, B. Geurts, H. Kuerten, Comparison of numerical schemes in large-eddy simulation of the temporal mixing layer, Int. J. Numer. Meth. Fluids 22 (1996) 297.
[12] X.D. Liu, S. Osher, T. Chan, Weighted essentially non-oscillatory schemes, J. Comput. Phys. 115 (1994) 200.
[13] G.S. Jiang, C.W. Shu, Efficient implementation of weighted ENO schemes, J. Comput. Phys. 126 (1996) 202.
[14] X. Zhong, High-order finite-difference schemes for numerical simulation of hypersonic boundary-layer transition, J. Comput. Phys. 144 (1998) 662.
[15] A.I. Tolstykh, M.V. Lipavskii, On performance of methods with third- and fifth-order compact upwind differencing, J. Comput. Phys. 140 (1998) 205.
[16] N.A. Adams, K. Shariff, A high-resolution hybrid compact-ENO scheme for shock–turbulence interaction problems, J. Comput. Phys. 127 (1996) 27.
[17] Z. Wang, G.P. Huang, An essentially nonoscillatory high-order Pade-type (ENO-Pade) scheme, J. Comput. Phys. 177 (2002) 37.
[18] S. Pirozzoli, Conservative hybrid compact-WENO schemes for shock–turbulence interaction, J. Comput. Phys. 178 (2002) 81.
[19] P. Beudan, P. Moin, Numerical experiments on the flow past a circular cylinder at a sub-critical Reynolds number, Report No. TF-62, Department of Mechanical Engineering, Stanford University, 1994.
[20] M.M. Rai, P. Moin, Direct simulations of transition and turbulence in a spatially evolving boundary layer, J. Comput. Phys. 109 (1993) 169.
[21] R. Mittal, P. Moin, Suitability of upwind-biased finite-difference schemes for large-eddy simulation of turbulent flows, AIAA J. 35 (1997) 1415.
[22] M. Breuer, Numerical and modeling influences on large eddy simulations for the flow past a circular cylinder, Int. J. Heat Fluid Flow 19 (1998) 512.
[23] E. Garnier, M. Mossi, P. Sagaut, P. Comte, M. Deville, On the use of shock-capturing schemes for large-eddy simulation, J. Comput. Phys. 153 (1999) 273.
[24] M. Mossi, P. Sagaut, Numerical investigation of fully developed channel flow using shock-capturing schemes, Comput. Fluids 31 (2002) 695.
[25] F. Ladeinde, X. Cai, M. Visbal, D.V. Gaitonde, Turbulence spectra characteristics of high order schemes for direct and large eddy simulation, Appl. Numer. Math. 36 (2001) 447.
[26] M. Meinke, W. Schroder, E. Krause, T. Rister, A comparison of second- and sixth-order methods for large-eddy simulations, Comput. Fluids 31 (2002) 695.
[27] J.P. Boris, F.F. Grinstein, E.S. Orans, R.J. Kolbe, New insights into large eddy simulation, Fluid Dyn. Res. 10 (1992) 199.
[28] C. Fureby, F.F. Grinstein, Large eddy simulation of high-Reynolds-number free and wall-bounded flows, J. Comput. Phys. 181 (2002) 68.
[29] M.S. Liu, C.J. Steffen Jr., A new flux splitting scheme, J. Comput. Phys. 107 (1993) 23.
[30] S.K. Lele, Compact finite-difference schemes with spectral-like resolution, J. Comput. Phys. 103 (1992) 16.
[31] B. Van Leer, Flux-Vector Splitting for the Euler Equations, Lecture Notes in Physics, vol. 170, Springer, New York/ Berlin, 1982, p. 507.
[32] M. Leisure, Turbulence in Fluids, Kluwer Academic Publishers, Dordrecht, 1987.
[33] C. Canuto, M.Y. Hussaini, A. Quarteroni, T.A. Zang, Spectral Methods in Fluid Dynamics, Springer, Berlin, 1988.
[34] S. Liu, C. Meneveau, J. Katz, On the properties of similarity subgrid-scale models and deduced from measurements in a turbulent jet, J. Fluid Mech. 275 (1994) 83.
[35] D. Carati, K. Jansen, T. Lund, A Family of Dynamic Models for Large-Eddy Simulation, Annual Research Briefs, Center for Turbulence Research, NASA Ames/Stanford Univ., 1995.
[36] G. Comte-Bellot, S. Corrsin, Simple Eulerian time correlation of full- and narrow-band velocity signals in grid-generated, 'isotropic' turbulence, J. Fluid Mech. 48 (2) (1971) 273.
[37] J.P. Chollet, in: L.J.S. Bradbury et al. (Eds.), Two-Point Closure Used for a Sub-grid Scale Model in Large Eddy Simulations, Turbulent Shear Flows, vol. 4, Springer, Berlin, 1985, p. 66.
[38] D. Lilly, A proposed modification of the Germano subgrid scale closure method, Phys. Fluids A 4 (1992) 633.
[39] J. Jiménez, On Why Dynamic Subgrid-Scale Models Work, Annual Research Briefs, Center for Turbulence Research, NASA Ames/Stanford Univ., 1995.
[40] B.J. Jin, N. Park, J.Y. Yoo, Large eddy simulation of boundary layer transition on the axial turbine blade by rotor induced wake, in: Proceedings of 2001 ASME Fluids Engineering Division Summer Meeting, 2001, FEDSM2001-18195.
[41] J.A. Ekaterinaris, Implicit, high-resolution, compact schemes for gas dynamics and aeroacoustics, J. Comput. Phys. 156 (1999) 272.
[42] R.M. Beam, R.F. Warming, An implicit factored scheme for the compressible Navier–Stokes equations, AIAA J. 16 (1978) 393.
[43] T.H. Pulliam, D.S. Chaussee, A diagonal form of an implicit approximate-factorization algorithm, J. Comput. Phys. 39 (1981) 347.
[44] M.R. Visbal, D.A. Gaitonde, High-order-accurate methods for complex unsteady subsonic flows, AIAA J. 37 (1999) 1231.

[45] T. Wei, W.W. Willmarth, Reynolds-number effects on the structure of a turbulent channel flow, J. Fluid Mech. 204 (1989) 57.
[46] J. Jeong, F. Hussain, On the identification of a vortex, J. Fluid Mech. 285 (1995) 69.
[47] G. Kravchenko, P. Moin, Numerical studies of flow over a circular cylinder at $Re_D = 3900$, Phys. Fluids 12 (2000) 403.
[48] S. Hahn, H. Choi, Unsteady simulation of jets in a cross flow, J. Comput. Phys. 134 (1997) 342.
[49] C. Norberg, Effects of Reynolds number, low-intensity free-stream turbulence on the flow around a circular cylinder, Publ. No. 87/2, Department of Applied Thermoscience and Fluid Mechanics, Chalmer University of Technology, Gothenburg, Sweden, 1987.
[50] L.M. Lourenco, C. Shih, Characteristics of the plane turbulent near wake of a circular cylinder, A particle image velocimetry study, private communication (data taken from [9]).
[51] L. Ong, J. Wallace, The velocity field of the turbulent very near wake of a circular cylinder, Exp. Fluids 20 (1996) 441.
[52] R.A. Clark, J.H. Ferziger, W.C. Reynolds, Evaluation of subgrid-scale models using an accurately simulated turbulent flow, J. Fluid Mech. 91 (1979) 1.
[53] H.S. Kang, S. Chester, C. Meneveau, Decaying turbulence in an active-grid-generated flow and comparisons with large-eddy simulation, J. Fluid Mech. 480 (2003) 129.
[54] C. Meneveau, Statistics of turbulence subgrid-scale stresses: necessary conditions and experimental tests, Phys. Fluids 6 (2) (1994) 815.
[55] J.L. Steger, R.F. Warming, Flux vector splitting of the inviscid gas dynamics equations with applications to finite difference methods, J. Comput. Phys. 40 (1981) 263.
[56] P.L. Roe, Approximate Riemann solvers, parameter vectors and difference schemes, J. Comput. Phys. 43 (1981) 357.
[57] R. Anderson, C. Meneveau, Effects of the similarity model in finite-difference LES of isotropic turbulence using a Lagrangian dynamic mixed model, Flow, Turbulence Combust. 62 (1999) 201.
[58] W. Anderson, J. Thomas, B. Van Leer, Comparison of finite volume flux vector splitting for the Euler equations, AIAA J. 24 (1986) 1453.
[59] A. Harten, B. Engquist, S. Osher, S. Chakravarthy, Uniformly high order accurate essentially non-oscillatory schemes III, J. Comput. Phys. 71 (1987) 231.